Evidence of rapid basalt dissolution in Southeastern US croplands

Ella Milliken*[1,2], Elliot Chang[3], Robert A Rioux[4], Isabella Chiaravalloti[1], Declan Miller[1], Ella Xu[1], Ben Brodin[3], Yoshiki Kanzaki[5], Christopher T. Reinhard[5], Noah Planavsky[1,2]

1. Earth & Planetary Sciences, Yale University, New Haven, CT, United States
2. Yale Center For Natural Carbon Capture, Yale University, New Haven, CT, United States
3. Lithos Carbon, Inc., Seattle, WA, United States
4. Yale School for the Environment, Yale University, New Haven, CT, United States
5. School of Earth and Atmospheric Sciences, Georgia Institute of Technology, Atlanta, GA, United States

*Corresponding Author: ella.milliken@yale.edu

Abstract

Enhanced weathering (EW) with crushed silicate rocks has been proposed as a potential form of carbon dioxide removal. This process requires relatively low capital cost, has high global implementation potential, and can provide agronomic and fertility co-benefits to landowners. However, to date, there are limited published, at-scale estimates of empirically constrained weathering rates on working farms. Here, we present estimates of ultrafine basalt enhanced weathering rates from an extended growing season based on over 1,800 samples from 24 fields across Southern Virginia and North Carolina, compared against 24 unapplied fields. This deployment utilizes a paired sample-resample design to constrain between-field heterogeneity, thereby reducing uncertainty. Area-weighted means of three soil mass balance approaches showed that 21.23 ± 7.44% (SEM) of the applied feedstock weathered in approximately six months, with an associated potential carbon dioxide removal of 3.79 ± 1.36 tCO_2 ha^{-1}. This value is consistent with weathering rates predicted from a first-order kinetic model driven by feedstock-specific properties.

Introduction

Within the past decade, there has been a growing interest in developing and deploying carbon dioxide removal (CDR) pathways to help meet global climate mitigation targets and as a way to tackle legacy anthropogenic greenhouse gas emissions (1–3). To date, billions of dollars have been invested in building the public and private infrastructure necessary for removing CO_2 at the gigaton-scale (3–5). With this growth, it has become increasingly important to accurately constrain the expected capacity of CDR solutions with respect to both deployment volume and capital requirements.

Enhanced weathering (EW) is a durable geochemical method of CDR, relying on the spreading and subsequent dissolution of fine-grained, cation-rich feedstocks in soil systems, which releases base cations and alkalinity into the environment (6) and can drive the conversion of CO_2 to bicarbonate (HCO_3^-) (7–9). Silicate weathering can also decrease acid export from soil systems, which impacts CO_2 fluxes from downstream rivers (10, 11). The use of alkaline feedstocks as a pH management strategy is a common agricultural practice, with the most common amendment being limestone. EW deployment seeks to optimize, subsidize, and expand this practice to remove appreciable quantities of CO_2 each year, with US projections as high as 0.5 $GtCO_2$ yr^{-1} (12). EW utilizes existing infrastructure (e.g., mines, industrial waste, and spreading equipment), enabling it to scale at a much lower cost than other geochemical CDR strategies (13). Further, EW offers key co-benefits provided to participating landowners and farmers, both through direct agronomic benefits and practice subsidization (1, 14–17).

Despite this potential, there are major uncertainties in estimates of the scale at which EW can be deployed (18). A key gap in our understanding of EW with silicates remains empirical constraints on the rates of

feedstock dissolution expected on working farms with optimal feedstocks (19–21). There have been consistent advances in modeling EW over the past decade, but the range of expected capacity is large (18, 22, 23). Thus, there is an obvious need to further constrain these estimates through empirical rate determinations from field deployments, and there has been considerable recent work pursuing academic EW field trials and mesocosm experiments with the aim of understanding and quantifying dissolution rates across settings (16, 24–30). These trials, however, remain limited in their ability to robustly mimic field conditions on working farms.

Solid-phase mass balance approaches have long been used to estimate natural weathering rates (31, 32), and, more recently, have been proposed to be useful for tracking enhanced weathering rates (33–35). Soils are spatiotemporally heterogeneous; their method of formation (i.e., the weathering of local rock, incorporation and decomposition of organic matter, and reliance on local water fluxes), and variable interactions with local climate and biogeochemistry through time, can lead to entirely different compositions from centimeter to meter scales (36, 37). Without a proper soil sampling procedure, it can be difficult to resolve signal from noise, which remains a significant challenge in attempts to quantify feedstock dissolution rate. However, methods for addressing spatial variability in soil sampling have been well-established in both agronomic and contaminant studies (37). While soil mass balance has been demonstrated to be possible in controlled settings, there are limited published weathering estimates from at-scale field trials (17, 33–35). Despite the lack of results, there have been questions about the ability of soil mass balance approaches to overcome signal-to-noise issues on working lands (e.g., 39). This has created an 'infeasibility assumption' that could curb efforts to empirically track the EW process, an issue similar to that confronted by attempts to track changes in SOC stocks.

The lack of documented field trials has hindered our understanding of where EW might be most efficiently deployed. While it is well understood that tropical and sub-tropical climates will be most conducive to high initial silicate dissolution rates, there has been very little empirical work on expected rates, especially for US-based climates. With over 20 million cultivated acres, the Southeastern US is already a major crop production area and is biogeochemically primed to serve as an EW hub (40). Its subtropical and tropical climates are expected to encourage rapid dissolution of feedstocks, while the low cation exchange capacity (CEC) of baseline soils has the potential to rapidly export cations with low time lags and lower risk of secondary mineral formation within the soil column (41). The Southeastern US is also a prime region that could benefit from enhanced weathering; this region is projected to see a 20-40% decline in yield within the next 75 years due to climate change (42). Declines in productivity are largely driven by the prevalence of highly degraded, acidic soils, caused by poor parent material, high drought risk, low water holding capacity, and low regenerative practice implementation (further exacerbated by high costs and low regional amendment availability) (43). Thus, the predicted effects of EW—increasing soil pH, micronutrient concentrations, and water retention, as well as providing direct yield benefits (12, 44, 45)—have the potential to significantly increase the agronomic and economic resilience of this region to climate change.

Here, we present a solid-phase mass-balance analysis from roughly 50 fields, half treated with basalt and half left as controls, in Southern Virginia and North Carolina, key regions in Southeastern US agriculture (Figure 1, Table 1). Both basalt and control fields exhibit equivalent variance in agronomic properties, suggesting that they are cross-comparable datasets with respect to baseline traits (SI Table 1-2). We show that using sample composites, matched spatial sampling over time, and multi-field aggregation can overcome the signal-to-noise challenges of soil geochemical mass-balance. We provide measured rates of basalt dissolution from multiple methods of dissolution quantification, using both full cation accounting (FCA) and immobile-element tau corrections (31) via aluminum (Al) and titanium (Ti). We also provide the associated potential carbon dioxide removal (pCDR) from this dissolution based on feedstock chemistry. Finally, using these empirical values we demonstrate the applicability of an average treatment effect framework for reducing uncertainty in CDR estimates across large deployment areas, while grounding the observed estimates using a first-order kinetic dissolution model.

Results and Discussion

In total, 1809 samples were used for analysis across 24 basalt-amended fields, and 1563 samples were used for analysis across 24 unapplied fields. Each sample contains 8-10 cores from within a 1 m radius following common agricultural sampling protocols [e.g., (37, 46–48)], coordinate matched using a 5.6 x 4.5 m grid pairing. All experimental fields were amended with a basalt from the same quarry in Butner, North Carolina, at a rate of approximately ~45 t ha^{-1}. The basalt has a p80 of 89.92 um, a BET specific surface area of 5.24 g m^{-2}, and a composition of 67% plagioclase, 13% augite/diopside, 8% volcanic glass, 4.3% olivine, and 4.9% enstatite, yielding a maximum CDR potential of 0.383 tCO_2 per ton of rock. Samples were taken prior to amendment (baseline; BL), within 3 weeks after basalt application (post-application; PA), and then resampled after harvest, approximately 6 months after initial application (resampling; RS). Maps of fields and sampling locations can be found in the supplement.

A critical assumption of the sample-resample mass balance approach is that the samples taken from the same georeferenced location are comparable in composition. Al/Ti ratios, a common provenance tracer (31, 32, 49), were used in this case to ensure sample fidelity over time, enable a relative cross-comparison of different sampling points, and avoid regression-to-the-mean phenomena. On a per-sample basis, the basalt-applied sample ΔAl/Ti shifted 3.32 ± 13.41%, and the control sample ΔAl/Ti shifted 0.33 ± 28.59 % (error presented as standard error of the mean) (Fig. 2a). Both basalt and control fields showed no bulk shift in Al/Ti ratios with resampling, although the high variance indicates that this assumption doesn't always hold on the individual sample level. This points to the importance of investigating the average effect at the field scale, rather than effects at the individual sample level, to overcome signal-to-noise concerns.

To properly demonstrate treatment effects, it is critical to develop a robust counterfactual scenario using densely sampled, comparable control fields. This ensures that any observed weathering signal is related to the implemented practice rather than to measurement error or an extraneous management effect (39, 50). Critically, control fields showed no significant shift in cation concentration (Fig. 2b; SI Fig. 2). This suggests that, under normal conditions, fields with no basalt application do not show any observed false-positive signal from sampling noise; further, this demonstrates that background weathering rates in the upper portion of degraded soils in the Southeast are below the observable limit of detection.

In contrast to control fields, basalt-applied fields showed clear signals of basalt application, indicated by significant increases in solid-phase cation concentrations following application ($p < 0.0001$), both in absolute cation values and when compared with Ti concentrations (Fig. 2c-d; SI Figures 3-26). While the statistical significance of signals at the RS timepoint varied between fields (SI Figures 3-26), there is a clear, statistically significant signal at the project level. This signal implies that geochemical mass balance can potentially resolve the treatment effect of basalt addition, despite the heterogeneity of local soil environments and of feedstock application itself. As a first step, this validates the use of geochemical mass-balance at the project level and suggests that paired soil sample-resample approaches can overcome signal-to-noise concerns.

Following the post-harvest resampling event, basalt weathering rates were calculated using per-sample bootstrapping, resulting in dissolution estimates that were largely consistent between the FCA and tau-corrected methods, albeit with deviations on individual fields (SI Figure 27). There are clear instances in which the tau-corrected rate, using Ti and Al as immobile tracers to correct for bulk density, varies with the FCA weathering rate (SI Fig. 3-27). Because Al and Ti are largely immobile elements in these soils, the variation in these signals on an individual sample level will be impacted by local sampling heterogeneity as well as local changes in soil bulk density. There are multiple methods of immobile tracer correction; in this case, we are normalizing shifts in Al and Ti concentration to the original empirical value (33, 35, 51). This assumes that the sampling of baseline conditions is a reasonable estimation of

baseline values, which appears valid based on the stability of the control fields across sampling timepoints (Fig. 2a-b).

Weighting by relative field area, basalt weathering rates estimated from FCA results yield relative dissolution percentages of 20.75 ± 7.54%, compared to an Al tau-corrected value of 21.01 ± 6.93% and a Ti-corrected value of 21.92 ± 7.85% across all 24 fields (error is presented as standard error of the mean). These values demonstrate a clear signal of basalt weathering in the Southeastern US on timescales relevant to growers and carbon credit markets, and are in line with both observations from other commercial deployments and from global models of potential weathering fluxes (17). When factoring in the tonnage applied to the fields, the mean estimate of potential carbon dioxide removal (pCDR) from FCA is 3.72 ± 1.39 tCO_2 ha^{-1}, compared to an Al-corrected rate of 3.74 ± 1.26 tCO_2 ha^{-1} and a Ti-corrected rate of 3.90 ± 1.42 tCO_2 ha^{-1}. However, we emphasize that the presented weathering rates should not be conflated with net CDR, as process emissions (52) and downstream carbon leakage (53) also need to be evaluated in any claim of durable carbon removal.

To understand the merits of measuring the average treatment effect, as compared to the effect at an individual field scale, we applied a bootstrapped mean-of-means approach to aggregate field-derived pCDR values, with project-level standard deviations derived using relative area weighting. The aggregation of fields using a bootstrapped means approach clearly leads to a reduction in error associated with mean values (Fig. 3a-c). As the gross sample size and acreage increase, the range of mean estimates becomes more indicative of the average treatment effect, and the relative uncertainty associated with the magnitude of the treatment effect decreases. This supports the assertion (39, 50, 54) that regional or project-level estimates can provide a more reliable mean effect relative to approximations made at smaller spatial scales.

We can further ground the approximate magnitude of the measured weathering rate using a simplified kinetic dissolution model. The modeling was conducted as a forward simulation (i.e. no calibration against measured bulk basalt dissolution) and included a Monte-Carlo based uncertainty propagation of baseline soil pH (5.1-6.1), mean annual soil temperature, and slight variability in mineralogical phases to ascertain a range of expected weathering rates (SI Fig. 28). The simulations utilize a component additivity framework, which allows for the simulated dissolution of individual mineral fractions. From this forward simulation of isolated mineral phases with associated surface-area-normalized rates, the model yields a mean estimate of 5.61 [3.88, 7.34] (error reported as standard deviation) tCO_2 ha^{-1} at 6 months, which bounds but is slightly higher than the measured in-field estimates reported above. We note that the simplified model assumes far-from-equilibrium reactive mineral phases and its basic formulation is likely most useful as a first-order estimate of weathering during dissolution of freshly spread basalt rather than a skilled prediction of dissolution at any given location. As the weathering process progresses, we expect the model to become less applicable given uncertainties in surface area evolution and the potential for feedstock mineral surface passivation. However, the relatively close agreement between the simulated weathering rates and the measured values suggests that we are observing reasonable rates and indicates that weathering systems can remain in a far-from-equilibrium state 6 months after feedstock application.

As shown in Figure 4, we observe clear deviations between measured rates and the simple dissolution model at the field scale. Fields, or clusters of fields, can demonstrate an unrealistically high or low rate, both of which are likely driven by spatial noise (38). However, when measuring the average treatment effect at the project level (50 fields in this case), the mean estimate falls within the model's ± 1 SD range (Fig. 4). This is a clear illustration of the potential problems associated with carbon accounting at the field scale.

Climate, plant activity, and soil management all play important roles in increasing the weathering rates across this region, compared to more temperate regions or mesocosm estimates (55–58). The average summer (June-September) temperature from 2024-2025 across the Southeast was 26.3°C, with average

summer precipitation of approximately 610 mm. These weathering rates are higher than other quantified estimates, highlighting that small-scale experiments may not ideally replicate real-world conditions (55–58). Weathering rates are driven by active soil environments, with high temperature and precipitation; thus, the assumption that weathering rates from the growing season will be mirrored in the winter is unlikely. We expect that the provided values will encompass the majority, if not all, weathering occurring in this agroecosystem over the course of the year, despite estimates being taken over only a portion of the year.

More broadly, the presented values are in line with published global estimates in subtropical and tropical environments, as well as reactive transport model (RTM) estimates for this region (Fig. 4, SI Table 3); (15–17, 22, 28, 29, 59–63). Notably, many published estimates are lower than what was empirically estimated by this study. This may in part be driven by a reliance on short-term mesocosms to supply training data for the RTMs, potentially leading to an underestimation of weathering rates. In any case, our results emphasize the need to construct large-scale datasets on working fields for the calibration and validation of predictive models.

Our results indicate that with controls and optimized sampling methodologies, soil mass balance approaches can yield reproducible rate estimates that are in line with existing observations and general kinetic bounds. Project-level estimates allow us to overcome signal-to-noise issues and generate an average treatment effect with a reduced uncertainty. Enhanced weathering has shown promise as a CDR strategy, while concurrent co-benefits to growers make it an appealing target for investment (13, 16, 17). However, it is inherently reliant on the rapid dissolution of feedstock, which must be constrained through empirical estimates and may only emerge in specific regions and contexts. Our results provide motivation to continue investment in empirically constraining weathering rates across scales in EW deployments, both within the Southeast and across the globe. As has been stressed extensively, it will be important to concurrently invest in work aimed at quantifying alkalinity and carbon fluxes after feedstock dissolution in the field (64–68). Nevertheless, these results, coupled with strong evidence for agronomic and economic benefits in the same region, provide additional impetus to explore EW as a land management practice that can potentially benefit farmers and help to reduce the climate impacts of agriculture (45).

Tables and Figures:

Table 1. Site properties for presented applied fields.

Site Name	lat [deg]	long [deg]	Size (ha)	Application Rate (dry metric tons/ha)	Reported Crop	# Samples
A	36.83	-78.38	19.09	44.49	Corn	19
B	36.81	-78.43	14.36	44.49	Corn	14
C	36.76	-78.48	27.05	44.49	Corn	26
D	36.72	-78.42	43.19	44.49	Corn	39
E	36.67	-78.49	5.04	45.695	Soybeans	54
F	36.83	-78.38	19.09	44.49	Corn	18
G	36.55	-78.60	38.26	38.16	Soybeans	28
H	36.31	-79.46	18.14	46.48	Hay	13
I	36.28	-78.72	27.39	49.33	Tobacco	28
J	36.42	-78.35	17.66	42.87	Grain Sorghum	20
K	36.42	-78.30	29.63	42.87	Grain Sorghum	17
L	36.40	-78.30	15.65	42.87	Grain Sorghum	32
M	35.99	-78.79	13.26	55.89	Hay / Pasture	22
N	36.35	-78.23	36.04	45.06	Pasture	32
O	35.83	-78.19	23.62	44.17	Hay	23
P	35.70	-78.54	21.45	43.42	Hay	21
Q	35.75	-78.47	16.21	43.42	Hay	15
R	35.73	-78.45	47.15	42.64	Cotton	43
S	35.68	-78.42	18.77	49.39	Soybeans	15
T	35.59	-78.39	35.32	49.39	Soybeans	30
U	35.47	-78.05	21.51	49.44	Soybeans	16
V	35.51	-78.00	30.76	49.44	Soybeans	30
W	35.48	-78.00	32.58	49.44	Soybeans	29
X	35.45	-77.99	20.15	49.44	Soybeans	19

Table 2. Mean individual site weathering values and associated potential carbon removal values. Error is given as SEM.

Site Name	Fw, cat. acct.	Fw, Al-tau	Fw, Ti-tau	tCO_2, cat. acct.	tCO_2, Al-tau	tCO_2, Ti-tau
A	5.67 ±13.29	5.51 ± 9.08	9.37 ± 13.53	0.97 ± 2.27	0.94 ± 1.55	1.60 ± 2.31
B	0.56 ± 13.83	-8.50 ± 13.44	-14.22 ± 20.54	0.10 ± 2.36	-1.45 ± 2.29	-2.42 ± 3.50
C	-32.57 ± 11.18	-17.21 ± 8.14	-29.85 ± 10.89	-5.55 ± 1.87	-2.93 ± 1.36	-5.09 ± 1.82
D	-3.35 ± 9.49	9.46 ± 11.72	-17.98 ± 13.67	-0.57 ± 3.31	1.61 ± 3.24	-3.06 ± 4.91
E	20.25 ± 4.86	17.14 ± 4.30	15.60 ± 5.60	3.54 ± 0.85	3.00 ± 0.75	2.73 ± 0.98
F	-6.01 ± 9.36	-12.07 ± 8.85	0.25 ± 9.21	-1.03 ± 1.60	-2.06 ± 1.51	0.04 ± 1.58
G	25.49 ± 20.69	32.23 ± 26.41	28.94 ± 24.27	3.73 ± 1.51	4.71 ± 1.93	4.23 ± 1.77
H	52.99 ± 7.94	60.19 ± 7.48	61.88 ± 8.29	9.43 ± 1.36	10.72 ± 1.28	11.02 ± 1.42
I	18.94 ± 10.17	26.85 ± 7.58	4.65 ± 11.47	3.58 ± 1.89	5.07 ± 1.41	0.88 ± 2.13
J	37.21 ± 6.85	35.29 ± 6.09	32.44 ± 6.89	6.11 ± 1.12	5.79 ± 1.00	5.33 ± 1.13
K	44.26 ± 7.60	44.15 ± 9.95	47.52 ± 8.24	7.27 ± 1.25	7.25 ± 1.63	7.80 ± 1.35
L	13.04 ± 8.05	23.45 ± 6.49	10.62 ± 11.37	2.14 ± 2.22	3.85± 1.73	1.74 ± 2.45
M	50.46 ± 7.19	32.68 ± 7.62	36.20 ± 9.37	10.80 ± 1.54	6.99 ± 1.63	7.75 ± 2.01
N	34.37 ± 7.35	27.42 ± 9.15	40.95 ± 7.05	5.93 ± 1.27	4.73 ± 1.58	7.07 ± 1.22
O	28.59 ± 8.44	26.58 ± 7.83	27.33 ± 9.82	4.84 ± 1.43	4.50 ± 1.32	4.62 ± 1.66
P	23.26 ± 8.49	21.62 ± 7.95	29.72 ± 8.18	3.87 ± 1.41	3.59 ± 1.32	4.94 ± 1.36
Q	-3.78 ± 11.33	-9.43 ± 11.85	8.85 ± 9.67	-0.63 ± 1.82	-1.57 ± 1.90	1.47 ±1.55
R	5.29 ± 6.80	-3.58 ± 7.95	14.91 ± 7.45	0.86 ± 1.11	-0.58 ± 1.30	2.44 ± 1.22
S	54.16 ± 6.25	47.38 ± 5.15	52.48 ± 6.42	10.24 ± 1.18	8.96 ± 0.98	9.93 ± 1.21
T	64.80 ± 4.87	61.67 ± 5.01	63.71 ± 5.51	12.26 ± 0.92	11.66 ± 0.95	12.05 ± 1.04
U	45.30 ± 5.32	40.00 ± 5.04	45.90 ± 5.81	8.58 ± 1.01	7.57 ± 0.95	8.69 ± 1.10
V	19.46 ± 7.75	24.27 ± 7.26	27.12 ± 7.90	3.68 ± 1.39	4.60 ± 1.30	5.14 ± 1.42
W	-5.81 ± 6.24	-2.40 ± 5.64	4.28 ± 7.03	-1.10 ± 1.18	-0.46 ± 1.07	0.81 ± 1.33
X	36.31 ± 8.56	32.60 ± 7.59	39.83 ± 8.59	6.88 ± 1.62	6.17 ± 1.44	7.54 ± 1.63

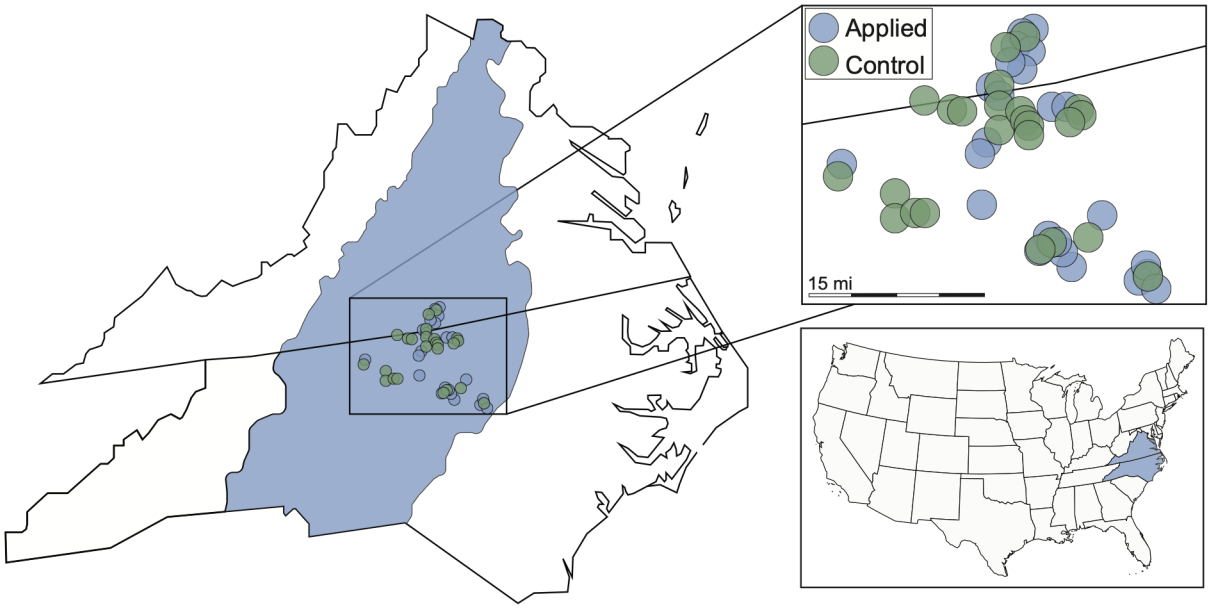

Figure 1. Site locations in North Carolina and Southern Virginia for 2024 and 2025 deployment fields. Sites are within 80 miles of each other, and all face similar temperature and precipitation regimes. The rough boundaries of the Piedmont area for North Carolina and Virginia are highlighted in blue.

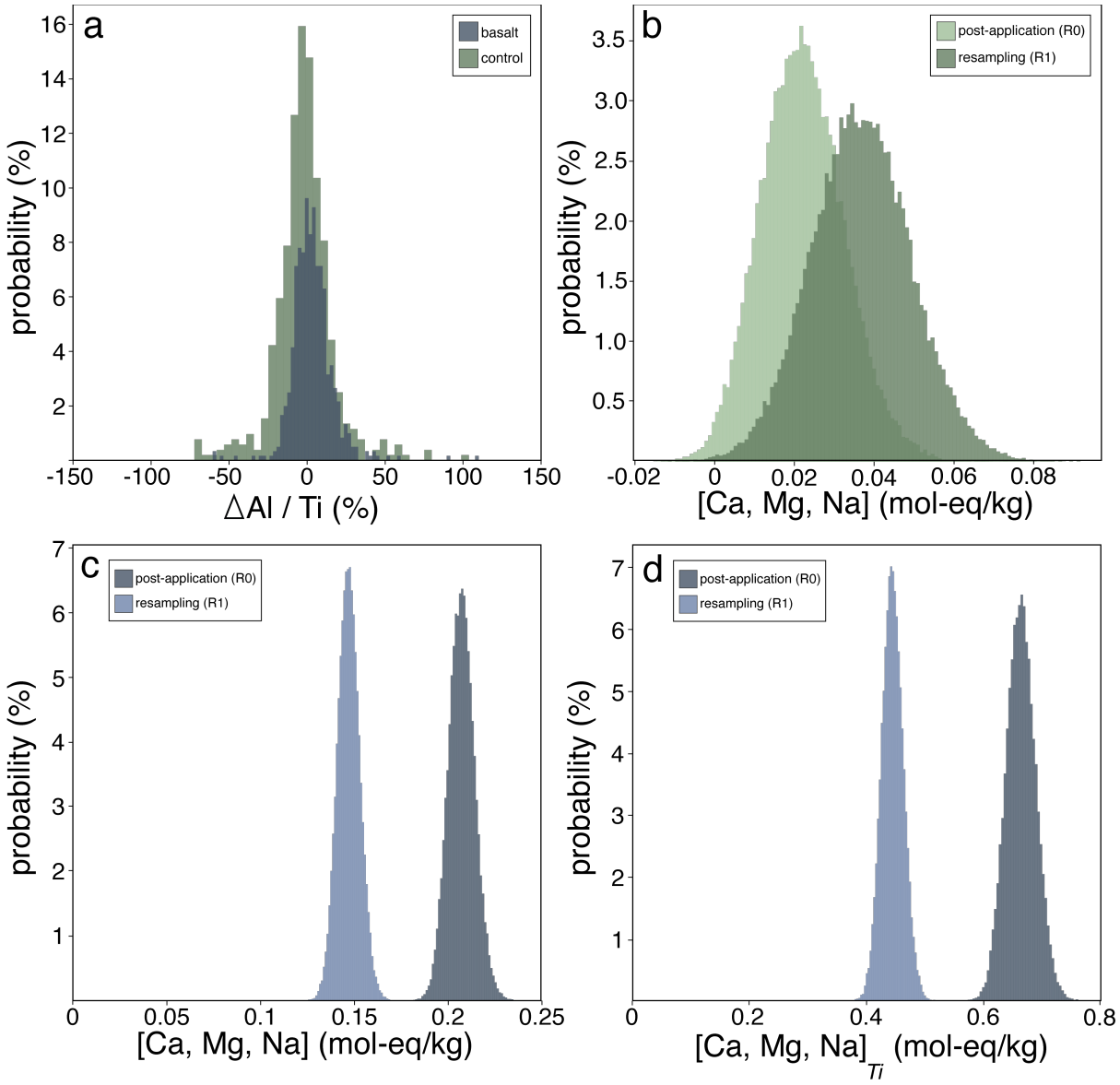

Figure 2. Bootstrapped distributions of cation and immobile tracer shifts for control and basalt-amended fields following baseline sampling. The values shown for each graph were calculated on a sample-by-sample basis by subtracting out baseline (BL) cation and Ti concentrations from subsequent resampling concentrations (RS and PA), then a bootstrap simulation (n = 50,000) was run on the aggregated population. Basalt timepoints for post-application (PA) and resampling (RS) are shown in blue, and control timepoints are shown in green. (a) % shift in Al/Ti ratio between the post-application and resampling timepoint for basalt and control fields. There was no significant difference in population shift ($p > 0.05$). (b) Aggregated molar-equivalence soil cation concentration for control sampling timepoints. There was no significant shift in population across PA and RS timepoints (n = 521; $p > 0.05$). (c) Aggregated molar-equivalence soil cation concentration for basalt-amended sampling timepoints. There was a significant shift in population across PA and RS timepoints (n = 603; $p < 0.0001$). (d) Aggregated molar-equivalence soil cation concentration for basalt-amended sampling timepoints, divided by respective Ti-concentration. There was a significant shift in population across PA and RS timepoints (n = 603; $p < 0.0001$).

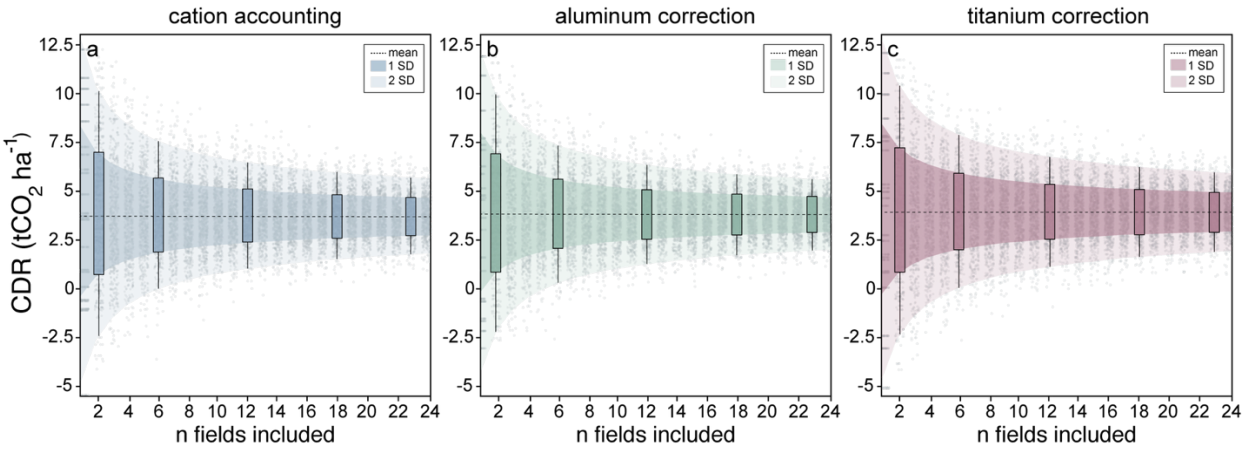

Figure 3. Bootstrapped (with replacement) area-weighted mean downsampling of individual fields for (a) FCA, (b) Al tau-corrected approach, and (c) Ti tau-corrected approach. Individual simulations are shown with gray dots, with the true mean shown with the black dashed line for each method. Two standard deviations of simulations are shown for each *n* value. The standard deviations for *n* = 2, 6, 12, 18, and 23 are shown in the darker boxes for each method. The introduction of increased acreage and field estimations led to a convergence of error towards the true population value. All mean estimates of simulations yield a mean within ± 0.2 tCO_2 ha^{-1}.

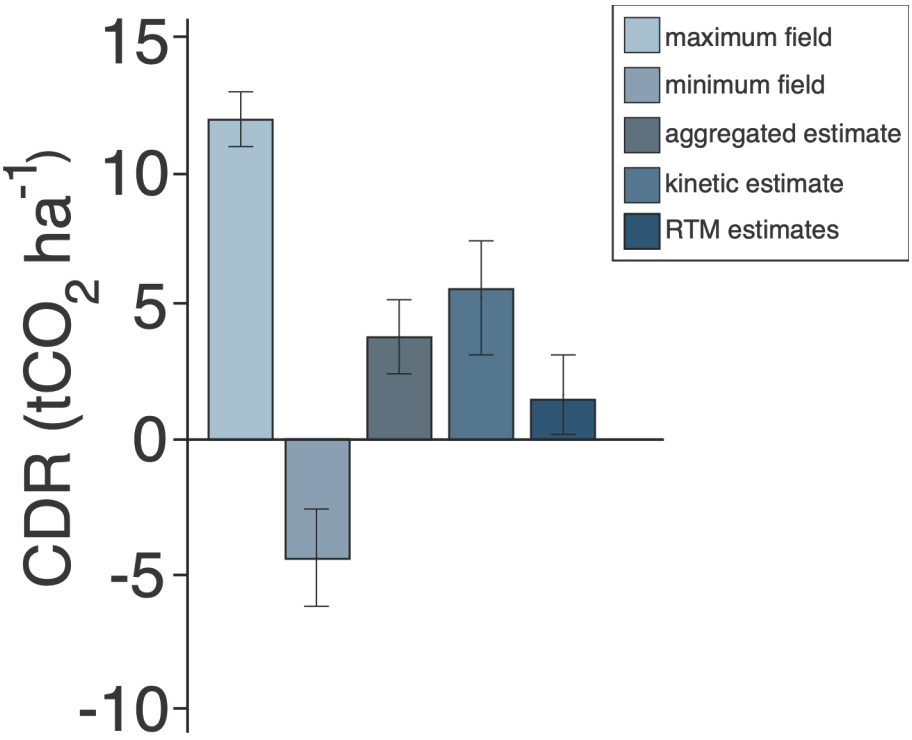

Figure 4. Comparison of per-hectare averaged CDR estimations for the field with the highest weathering signal, the field with the lowest weathering signal, the aggregate signal from all fields, the first-order kinetic model estimate, and averaged regional RTM estimates. Individual RTM estimates are listed in SI Table 3. Error of the empirical estimations is presented as SEM.

Acknowledgements

The authors acknowledge funding from Microsoft to deploy this EW project. We thank the Lithos operational team for logistic support. NJP acknowledges support from the Foundation for Science and Technology.

Competing Interest Statement: N.J.P and C.T.R. were co-founders of Lithos Carbon but have no remaining ties to the company. The remaining authors declare that they have no competing interests.

Materials and Methods

Deployment and Sampling Design

All fields used in this analysis are in North Carolina and Southern Virginia, within the Piedmont region (Figure 1). Fields used had consistent management regimes, high sample counts, reasonable field-wide heterogeneity, and high acreage. To provide participating farms with anonymity, exact locations are not listed, though rough coordinates of each site, as well as site properties, are shown in Table 1. All fields, both controls and deployments, were within 80 miles of each other (Figure 1). Treatment sites received approximately 50 metric tons ha^{-1} of basalt feedstock (Table 1). Control fields received no feedstock amendment and had unchanged management practice with respect to their co-located treatment areas. Full maps of each field, showing spatial distribution of farm area and soil sampling locations, are provided in the supplement. All sampling and deployment data has been collected and provided by Lithos Carbon.

Soil sampling followed a spatially systematic design intended to resolve enhanced weathering signals against inherent agricultural soil variability. Field boundaries were first digitized from grower-reported field maps using QGIS (v3.44), and sampling locations were then generated within these boundaries using a 2.5-acre density jittered grid applied across both treatment and control fields. The jittered design provided distributed spatial coverage while avoiding strict alignment with planting rows or commercial agricultural management features.

Control fields, which received no basalt amendment, were designated prior to deployment using a representation-based framework. Stratification considered crop type, soil texture class, management history (e.g., liming, fertilizer inputs, tillage), landscape position, and geographic separation of field blocks. Control acreage was embedded across the broader deployment footprint and allocated proportionally across relevant crop and management strata to preserve climatic and agronomic comparability. Furthermore, controls were assigned at the field level rather than as sub-field strips within treated areas to minimize cross-field contamination and management interference.

Sampling coordinates were generated in advance in accordance with the sampling design framework and uploaded to a GNSS-enabled field data collection platform. Field navigation and point collection used a Trimble DA2 GNSS receiver paired with TerraFlex software, enabling ≤30 cm horizontal accuracy prior to sampling. At each sampling event, the as-sampled coordinate corresponding to the composite sample center was recorded to document field-realized positioning under operational constraints. Where a predefined location was obstructed or not practically collectible, the nearest representative location was sampled and the updated coordinate recorded.

Soil Sampling

At each georeferenced location, soils were collected as a composite sample representing the cultivated topsoil layer (0–15 cm). Each composite consisted of eight individual cores collected within approximately a 1.5 m radius of the central coordinate using a drill-mounted auger. Cores were homogenized in a collection

bucket prior to subsampling. Composite sampling was selected to reduce microscale heterogeneity and improve signal-to-noise ratios in structured agricultural soils relative to single-core sampling approaches. Each composite was split into two labeled subsamples in the field to support parallel laboratory workflows, with one subsample designated for geochemical analysis (i.e. elemental cation measurements) and the other for agronomic analysis (i.e. soil property measurements). All fields were sampled prior to basalt application to provide a baseline (BL) set of measurements. Fields were then sampled within 2 weeks post-application (R0) and additionally resampled between 3-6 months after application (R1) to quantify weathering progression.

Feedstock Characterization

All fields were applied with Sunrock Basalt ($Al_{0.41}Fe_{0.11}(Mg_{0.16}Ca_{0.14})Si_{1.17}O_2$), sourced from Butner, North Carolina. Feedstock information can be found in the supplement (SI Figure 1).

Soil Analysis

Following aggregation, soils were dried in an oven overnight at 60°C and pulverized until >85% of the pulverized material passed No. 200 mesh (75 µm diameter). Samples were analyzed by ALS Laboratories. For full geochemical processing, the pulverized soils were digested using a lithium-borate fusion. This involved mixing the material with a lithium meta-borate fluxing agent and heating it in a muffle furnace at 1,000°C to create a molten lithium-borate salt. The molten samples were immediately dissolved in a nitric acid solution for characterization via inductively coupled plasma (ICP) mass spectrometry (MS) for trace elements (e.g. Ti, Cr, La, Nd, etc.) and optical emission spectroscopy (OES) for major elements (e.g. K, Na, Mg, Ca, Al, etc.). All analyses included quality control checks against certified reference materials for heavy metals including rare earth elements. Blank samples were analyzed in triplicate between batches of analytes. Cations (Ca, Mg, Na) were converted and aggregated to a single molar-equivalent concentration for each sample (eq cation/kg soil). Aluminum (Al) concentration was derived from Al_2O_3 data. Titanium (Ti) concentration was derived from TiO_2 data.

Data Analysis

Bootstrapped Plotting and Data Aggregation: Each treatment sample's coordinates were assigned to a cell using a fixed global grid, and then converted using 1° longitude = 111,320 m. Each grid cell in ground distance units therefore equates to 5.6m x 4.5m (height x width). All BL, PA, and RS samples were assigned to a grid cell, and any replicate samples falling within the same grid cell at the same time point were averaged before further analysis was conducted. Each grid cell was assigned a field key based on its metadata information (operational documentation of deal_id, farm_id, and field_id supplied by Lithos), resulting in a total of 48 unique, geo-located fields.

Sample points within a single field are not truly independent due to their similar soil types, application rate of basalt, and agricultural management practices. As such, uncertainty was quantified with a non-parametric cluster bootstrap in which the field (not individual samples) was used as the unit of resampling. For each cluster size (N = 1 – 24 total fields), the simulation drew N fields with replacement from the total population of samples. The pulled samples were used to compute CDR based on full cation accounting (FCA) and tau quantification. This procedure was repeated 20,000 times. The bootstrap mean and standard deviation across replicates were reported as a function of N to evaluate population-level uncertainty changes as more fields are aggregated together. Mean and standard deviations were weighted using the relative area for each field.

Full Cation Accounting: For the full cation accounting (FCA) framework, the percent of feedstock dissolution was determined by comparing the total gain in concentration of molar-equivalent base cations (Ca, Mg, Na) between BL and PA, or the amount of added average concentration, to the concentration remaining at RS:

$$F_{w-FCA} = \frac{(PA - RS)}{(PA - BL)}$$

Tau Quantification: The tau quantification method utilizes classic principles of soil science (69–71). This method corrects for changes in bulk density using an immobile tracer, allowing for correction of weathering rate using a PA sample.

$$F_{w-Tau} = \left(1 - \frac{\frac{CAT_{RS}}{Ti_{RS}}}{\frac{CAT_{PA}}{Ti_{PA}}}\right) * \frac{CAT_{PA}}{(CAT_{PA} - CAT_{BL})}$$

In this method, ratios of CAT:IM, in this case Ti or Al, are compared at RS and PA timepoints. If the ratio decreases, this shows feedstock weathering at the RS timepoint. The caveat of this rate calculation is that it cannot be directly compared to a FCA rate, as τ is simply a ratio that must be multiplied by the total cations within the mean PA sample to give a proportion of loss. Both treatment and control tau ratios were determined using paired, nonparametric bootstrap on the mean of within-pair differences with 100,000 resamples, then multiplied by a mean PA concentration. Samples outside of 3 standard deviations of the mean were removed from analysis.

Notably, the form of tau quantification utilized in this analysis is not equivalent to the tracer-based mass-balance method advanced by Reershemius et al., 2023 (TiCAT), where CAT_{PA} is inferred by Ti_{RS}. The framework as originally designed was intended to protect against the influence of inconsistent recovery of feedstock powder across sampling events on dissolution interpretations, where under sampling of feedstock powder acts as a confounding variable for rock dissolution. Here, we assume the high number of samples across a relatively diverse set of fields controls against the possibility of systematic bias in feedstock recovery during the R1 sampling event. As such, we also avoid the asymptotic behavior common in tracer-based mass balance, which references the common form of tracer-based quantification, or TiCAT (51).

CDR Calculation and Comparison: The bootstrap FCA CDR was calculated by converting molar-equivalent cation loss between PA and RS events to tCDR/ha, assuming full charge-balance by bicarbonate. The FCA rate was done by multiplying the calculated % loss by the known application rate, determined by dividing the known delivered dry tons of rock by field area, then converting the molar-equivalent cation loss to tCDR/ha. The Al/Ti tau rates were derived by multiplying the Tau ratio by PA cation concentration, then converting the loss to tCDR/ha. Controls do not show a significant change and therefore are not subtracted from the rate. All error is reported in SEM.

First-Order Kinetic Modeling as Reference: Basalt dissolution rates were compared against a simple kinetic dissolution model using a component additivity approach. For each reactive basalt mineral phase detected via XRD, each mineral was assigned a pH-dependent surface dissolution rate that was Arrhenius-corrected from the 25°C reference state to the local annual mean soil temperature (72):

$$r_i(pH, T) = k_{acid,25} * e^{\frac{-E_{a,acid}}{R}*\left(\frac{1}{T} - \frac{1}{T_{ref}}\right)} * {a_{H^+}}^{n_H} + k_{neutral,25} * e^{\frac{-E_{a,neutral}}{R}*\left(\frac{1}{T} - \frac{1}{T_{ref}}\right)} \left[mol\ m^{-2}\ s^{-1}\right]$$

with $a_{H^+} = 10^{-\mathrm{pH}}$, $T_{\mathrm{ref}} = 298.15$ K (25 °C) and $R = 8.314$ J mol^{-1} K^{-1}. Palandri & Kharaka (2004; USGS OFR 2004-1068) was used to estimate log k and E_a for both mechanisms of the four crystalline silicates. The pH dependence for basaltic glass was derived from Wolff-Boenisch et al. (2004) and the activation energy was obtained from Gislason & Oelkers (2003) (log $k_{\mathrm{acid}} = -8.54$, $n_{\mathrm{H}} = 0.31$, $E_a = 25.5$ kJ/mol, no

neutral mechanism). At the acidic pH regime of the measured soils, the base (alkaline) mechanism was omitted for simplification.

The bulk lab-measured BET (5.24 m²/g) surface area was applied as the specific surface area of each reactive phase, mineral i ($BET_i = BET_{bulk}$). The per-mineral first-order rate constant and associated weathering fraction (F_w) are then:

$$k_i = BET_{bulk} * r_i(pH, T) * MW_i * \left(\frac{s}{yr}\right) [yr^{-1}]$$

$$F_{w,i}(t) = 1 - e^{-k_i * t}$$

Each mineral's cation-equivalent pool (eq / kg mineral) was also defined as:

$$P_i = \left(\frac{wt\%_i}{100}\right) * \left(\frac{1000}{MW_i}\right) * v_i$$

where v_i is the equivalents of base cations (Ca^{2+}, Mg^{2+}, Na^{+}) released per mole of mineral dissolved. Gross potential CO_2 removal was then obtained assuming one mole of CO_2 sequestered per equivalent of base cation released:

$$CO_{2,i}(t) = F_{w,i}(t) * P_i * L * M_{CO2} * 10^{-3} [tCO_2\ ha^{-1}]$$

$$CO_{2,i}(t)\ [tCO_2\ ha^{-1}] = F_{w,i}(t) \cdot P_i \cdot L \cdot M\_CO_2 \cdot 10^{-3}$$

Where L = 50,000 kg basalt ha^{-1} (50 t ha^{-1} feedstock spread) and M_{CO2} = 0.044 kg/mol. Mineral formulation, relative abundance (wt %), cation pool, and relative specific surface area are provided below:

Mineral	**Formula**	**wt % (mean ± SD, n = 3)**	**MW (g/mol)**	**ν (eq/mol)**	**SSA_i (m²/g)**
Plagioclase (lab. An60)	$(Ca_{0.6}Na_{0.4})(Al_{1.6}Si_{2.4})O_8$	67.07 ± 1.36	271.80	1.60	5.240
Augite/Diopside	$CaMgSi_2O_6$	13.20 ± 1.13	216.55	4.00	5.240
Olivine (Fo80)	$(Mg_{0.8}Fe_{0.2})_2SiO_4$	4.33 ± 0.45	153.31	4.00	5.240
Enstatite/Ferroan	$(Mg_{0.7}Fe_{0.3})SiO_3$	4.87 ± 0.55	110.00	2.00	5.240
Volcanic glass	$Si,Al_{0.36}Fe_{0.21}Mg_{0.28}Ca_{0.26}Na_{0.08}O_{3.45}$	8.33 ± 1.53	125.00	1.18	5.240

Per-mineral dissolution kinetics (25 °C reference) are outlined below:

Phase	**log k_{acid} (mol m^{-2} s^{-1})**	**n_H**	**$E_{a,acid}$ (kJ/mol)**	**log $k_{neutral}$**	**$E_{a,neutral}$ (kJ/mol)**	**Source**

Plagioclase (labradorite An60)	-7.87	0.626	42.1	-10.91	45.2	
Augite / diopside	-6.36	0.710	96.1	-11.11	40.6	(72)
Olivine (Fo80)	-6.85	0.470	67.2	-10.64	79.0	(72)
Basaltic (volcanic) glass	-8.54	0.310	25.5	—	—	(73, 74)
Orthopyroxene (En70)	-9.02	0.600	80.0	-12.72	80.0	(72)

Three independent sources of uncertainty were evaluated using Monte Carlo simulation. Baseline pH (field-to-field variability across the 1,559 soil samples), mineral relative abundance (three XRD analyses of the same feedstock), and between farm mean annual soil temperature were evaluated as the three most likely factors contributing to uncertainty in this simplified kinetic model. Per draw (N = 20,000), k_i and $F_{w,i}(t)$ were recomputed at the drawn pH, T, and P_i at the drawn relative mineral wt %. The per-mineral gross CO_2 removal values, $CO_{2,i}(t)$, were then assembled for each reactive phase and summed to provide the total CDR estimate.

References

1. S. Smith, *et al.*, The State of Carbon Dioxide Removal 2024 - 2nd Edition. (2024).

2. W. F. Lamb, *et al.*, The carbon dioxide removal gap. *Nat. Clim. Chang.* **14**, 644–651 (2024).

3. M. j. Mace, C. L. Fyson, M. Schaeffer, W. L. Hare, Large-Scale Carbon Dioxide Removal to Meet the 1.5°C Limit: Key Governance Gaps, Challenges and Priority Responses. *Global Policy* **12**, 67–81 (2021).

4. O. Edenhofer, M. Franks, F. Gruner, M. Kalkuhl, K. Lessmann, The Economics of Carbon Dioxide Removal. *Annual Review of Resource Economics* **17**, 301–321 (2025).

5. Intergovernmental Panel On Climate Change (Ipcc), Ed., *Climate Change 2022 - Mitigation of Climate Change: Working Group III Contribution to the Sixth Assessment Report of the Intergovernmental Panel on Climate Change*, 1st Ed. (Cambridge University Press, 2023).

6. J. Hartmann, *et al.*, Enhanced chemical weathering as a geoengineering strategy to reduce atmospheric carbon dioxide, supply nutrients, and mitigate ocean acidification. *Reviews of Geophysics* **51**, 113–149 (2013).

7. R. G. Hilton, A. J. West, Mountains, erosion and the carbon cycle. *Nat Rev Earth Environ* **1**, 284–299 (2020).

8. J. Gaillardet, B. Dupré, P. Louvat, C. J. Allègre, Global silicate weathering and CO2 consumption rates deduced from the chemistry of large rivers. *Chemical Geology* **159**, 3–30 (1999).

9. R. A. Berner, K. A. Maasch, Chemical weathering and controls on atmospheric O2 and CO2: Fundamental principles were enunciated by J.J. Ebelmen in 1845. *Geochimica et Cosmochimica Acta* **60**, 1633–1637 (1996).

10. P. A. Raymond, J. J. Cole, Increase in the export of alkalinity from North America's largest river. *Science* **301**, 88–91 (2003).

11. N.-H. Oh, P. A. Raymond, Contribution of agricultural liming to riverine bicarbonate export and CO2 sequestration in the Ohio River basin. *Global Biogeochemical Cycles* **20** (2006).

12. D. J. Beerling, *et al.*, Transforming US agriculture for carbon removal with enhanced weathering. *Nature* 1–10 (2025). https://doi.org/10.1038/s41586-024-08429-2.

13. D. J. Beerling, *et al.*, Challenges and opportunities in scaling enhanced weathering for carbon dioxide removal. *Nat Rev Earth Environ* **6**, 672–686 (2025).

14. F. Haque, R. M. Santos, A. Dutta, M. Thimmanagari, Y. W. Chiang, Co-Benefits of Wollastonite Weathering in Agriculture: CO2 Sequestration and Promoted Plant Growth. *ACS Omega* **4**, 1425–1433 (2019).

15. A. Vienne, *et al.*, Enhanced Weathering Using Basalt Rock Powder: Carbon Sequestration, Co-benefits and Risks in a Mesocosm Study With Solanum tuberosum. *Front. Clim.* **4** (2022).

16. D. J. Beerling, *et al.*, Enhanced weathering in the US Corn Belt delivers carbon removal with agronomic benefits. *Proc Natl Acad Sci U S A* **121**, e2319436121 (2024).

17. J. Jordan, *et al.*, Enhanced rock weathering for improved farmer welfare in the Global South: An at-scale case study for rice agriculture in India in (2025), pp. EGU25-18512.

18. D. J. Beerling, *et al.*, Challenges and opportunities in scaling enhanced weathering for carbon dioxide removal. *Nat Rev Earth Environ* **6**, 672–686 (2025).

19. S. Calabrese, *et al.*, Nano- to Global-Scale Uncertainties in Terrestrial Enhanced Weathering. *Environ. Sci. Technol.* **56**, 15261–15272 (2022).

20. M. O. Clarkson, *et al.*, A review of measurement for quantification of carbon dioxide removal by enhanced weathering in soil. *Front. Clim.* **6** (2024).

21. M. Schiedung, *et al.*, Uncertainties of enhanced rock weathering for climate-change mitigation. *Nat Rev Earth Environ* **7**, 253–266 (2026).

22. S. H. Baek, *et al.*, Impact of Climate on the Global Capacity for Enhanced Rock Weathering on Croplands. *Earth's Future* **11**, e2023EF003698 (2023).

23. L. A. Bullock, R. H. James, J. Matter, P. Renforth, D. A. H. Teagle, Global Carbon Dioxide Removal Potential of Waste Materials From Metal and Diamond Mining. *Front. Clim.* **3** (2021).

24. K. Kurokawa, *et al.*, Direct evidence for enhanced mineral weathering in cropland verified by quantitative X-ray powder diffraction. *Applied Geochemistry* **205**, 106869 (2026).

25. D. P. Maxbauer, *et al.*, Evidence for carbon dioxide removal via enhanced rock weathering with steel slag, though not basalt, in a midwestern U.S. field trial. *Front. Clim.* **7** (2026).

26. C. Dietzen, M. Rizzi, T. J. Suhrhoff, M. T. Rosing, Enhanced weathering of glacial rock flour drives coupled inorganic and organic carbon sequestration in a five-year field experiment. *EGUsphere* 1–27 (2026). https://doi.org/10.5194/egusphere-2026-2760.

27. X. Dupla, M. B. Bertagni, S. Grand, Three Years of Field Trials Indicate a Sustained Enhanced Rock Weathering Signal with Limited CO2 Removal. *Environ. Sci. Technol.* **59**, 25751–25764 (2025).

28. I. B. Kantola, *et al.*, Improved net carbon budgets in the US Midwest through direct measured impacts of enhanced weathering. *Global Change Biology* **29**, 7012–7028 (2023).

29. C. S. Larkin, *et al.*, Quantification of CO2 removal in a large-scale enhanced weathering field trial on an oil palm plantation in Sabah, Malaysia. *Front. Clim.* **4** (2022).

30. C. Dietzen, R. Harrison, S. Michelsen-Correa, Effectiveness of enhanced mineral weathering as a carbon sequestration tool and alternative to agricultural lime: An incubation experiment. *International Journal of Greenhouse Gas Control* **74**, 251–258 (2018).

31. G. H. Brimhall, W. E. Dietrich, Constitutive mass balance relations between chemical composition, volume, density, porosity, and strain in metasomatic hydrochemical systems: Results on weathering and pedogenesis. *Geochimica et Cosmochimica Acta* **51**, 567–587 (1987).

32. O. A. Chadwick, G. H. Brimhall, D. M. Hendricks, From a black to a gray box — a mass balance interpretation of pedogenesis. *Geomorphology* **3**, 369–390 (1990).

33. T. Reershemius, *et al.*, Initial Validation of a Soil-Based Mass-Balance Approach for Empirical Monitoring of Enhanced Rock Weathering Rates. *Environ. Sci. Technol.* **57**, 19497–19507 (2023).

34. T. J. Suhrhoff, *et al.*, A tool for assessing the sensitivity of soil-based approaches for quantifying enhanced weathering: a US case study. *Front. Clim.* **6** (2024).

35. T. J. Suhrhoff, *et al.*, An Updated Framework and Signal-to-Noise Analysis of Soil Mass Balance Approaches for Quantifying Enhanced Weathering on Managed Lands. *Environ. Sci. Technol.* **59**, 26440–26453 (2025).

36. An overview of soil heterogeneity: quantification and implications on geotechnical field problems. Available at: https://cdnsciencepub.com/doi/epdf/10.1139/t02-090 [Accessed 10 July 2026].

37. P. G. Lawrence, W. Roper, T. F. Morris, K. Guillard, Guiding soil sampling strategies using classical and spatial statistics: A review. *Agronomy Journal* **112**, 493–510 (2020).

38. B. Rogers, K. Maher, An uncertainty-aware framework for solid-phase measurement and verification of enhanced weathering. *Front. Clim.* **7** (2026).

39. M. A. Bradford, *et al.*, Testing the feasibility of quantifying change in agricultural soil carbon stocks through empirical sampling. *Geoderma* **440**, 116719 (2023).

40. USDA - National Agricultural Statistics Service Homepage. Available at: https://www.nass.usda.gov/ [Accessed 1 July 2026].

41. Y. Kanzaki, *et al.*, Soil cation storage as a key control on the timescales of carbon dioxide removal through enhanced weathering.

42. A. Hultgren, *et al.*, Impacts of climate change on global agriculture accounting for adaptation. *Nature* **642**, 644–652 (2025).

43. Soil and Water Conservation in the Southeastern United States: A Look at Conservation Practices Past, Present, and Future - Busscher - 2010 - SSSA Special Publications - Wiley Online Library. Available at: https://acsess.onlinelibrary.wiley.com/doi/10.2136/sssaspecpub60.c7 [Accessed 13 July 2026].

44. C. Feldhaus, M. Gleue, A. Löschel, P. Werner, The role of co-benefits in motivating climate change mitigation – Experimental evidence. *Ecological Economics* **239**, 108783 (2026).

45. E. Milliken, *et al.*, Significant yield benefits from basalt soil amendments in the Southeastern US. *CDRXIV* (2026).

46. Protocol - Composite Soil Sampling - MCSE. Available at: https://lter.kbs.msu.edu/protocols/188 [Accessed 8 September 2026].

47. Soil variability and collecting a representative sample | Science Societies. Available at: https://www.sciencesocieties.org/publications/crops-soils/2021/july-august/soil-variability-and-collecting-a-representative-sample [Accessed 8 September 2026].

48. S. H. Institute, How to Sample Soil for Accurate Results. (2026). Available at: https://soilhealthinstitute.org/news-events/how-to-sample-soil-for-accurate-results/ [Accessed 8 September 2026].

49. G. H. Brimhall, *et al.*, Quantitative geochemical approach to pedogenesis: importance of parent material reduction, volumetric expansion, and eolian influx in lateritization. *Geoderma* **51**, 51–91 (1991).

50. E. Potash, M. A. Bradford, E. E. Oldfield, K. Guan, Measure-and-remeasure as an economically feasible approach to crediting soil organic carbon at scale. *Environ. Res. Lett.* **20**, 024025 (2025).

51. I. Productivity, Enhanced rock weathering false-positive explorer | Mati Carbon. Available at: https://mati.earth/articles/enhanced-rock-weathering-false-positive-explorer [Accessed 7 August 2026].

52. J. Kroeger, B. Zhang, N. Planavsky, Y. Yao, Analyzing Co-Benefits and Rock Sourcing in Life Cycle and Techno-Economic Assessment of Enhanced Rock Weathering. *Environ. Sci. Technol.* **60**, 6215–6226 (2026).

53. Y. Kanzaki, N. J. Planavsky, C. T. Reinhard, New estimates of the storage permanence and ocean co-benefits of enhanced rock weathering. *PNAS Nexus* **2**, pgad059 (2023).

54. A. Polussa, *et al.*, Counterfactual designs for quantifying management effects on soil carbon change at multi-field scales. *Geoderma* **473**, 118007 (2026).

55. M. Abdalqadir, D. Hughes, S. Rezaei Gomari, U. Rafiq, A state of the art of review on factors affecting the enhanced weathering in agricultural soil: strategies for carbon sequestration and climate mitigation. *Environ Sci Pollut Res* **31**, 19047–19070 (2024).

56. S. Vicca, *et al.*, Is the climate change mitigation effect of enhanced silicate weathering governed by biological processes? *Global Change Biology* **28**, 711–726 (2022).

57. I. B. Kantola, M. D. Masters, D. J. Beerling, S. P. Long, E. H. DeLucia, Potential of global croplands and bioenergy crops for climate change mitigation through deployment for enhanced weathering. *Biol Lett* **13**, 20160714 (2017).

58. E. Milliken, A. Woodley, N. J. Planavsky, Direct Measurement of Carbon Dioxide Removal Due to Enhanced Weathering. *Environ. Sci. Technol. Lett.* **12**, 970–976 (2025).

59. Y. Tu, *et al.*, Scaling up enhanced rock weathering for equitable climate change mitigation. *Commun. Sustain.* **1**, 32 (2026).

60. D. S. Goll, *et al.*, Potential CO2 removal from enhanced weathering by ecosystem responses to powdered rock. *Nat. Geosci.* **14**, 545–549 (2021).

61. R. Khalidy, Y. W. Chiang, R. M. Santos, Reactive transport modeling of carbon capture in soil amended with fast weathering silicate minerals. [Preprint] (2024). Available at: https://www.researchsquare.com/article/rs-3851603/v1 [Accessed 9 August 2026].

62. M. E. Kelland, *et al.*, Increased yield and CO2 sequestration potential with the C4 cereal Sorghum bicolor cultivated in basaltic rock dust-amended agricultural soil. *Global Change Biology* **26**, 3658–3676 (2020).

63. A. L. Lewis, *et al.*, Effects of mineralogy, chemistry and physical properties of basalts on carbon capture potential and plant-nutrient element release via enhanced weathering. *Applied Geochemistry* **132**, 105023 (2021).

64. Y. Kanzaki, *et al.*, Soil cation storage is a key control on the carbon removal dynamics of enhanced weathering. *Environ. Res. Lett.* **20**, 074055 (2025).

65. D. J. Beerling, *et al.*, Challenges and opportunities in scaling enhanced weathering for carbon dioxide removal. *Nat Rev Earth Environ* **6**, 672–686 (2025).

66. S. Zhang, C. T. Reinhard, S. Liu, Y. Kanzaki, N. J. Planavsky, A framework for modeling carbon loss from rivers following terrestrial enhanced weathering. *Environ. Res. Lett.* **20**, 024014 (2025).

67. N. J. Planavsky, *et al.*, Bridging carbon removal time lags in agricultural enhanced weathering via methane emission reduction. *Environ. Res. Lett.* **21**, 121002 (2026).

68. T. Isson, A. J. West, Can enhanced alkalinity store carbon durably? *Science* **392**, 808–810 (2026).

69. O. A. Chadwick, G. H. Brimhall, D. M. Hendricks, From a black to a gray box — a mass balance interpretation of pedogenesis. *Geomorphology* **3**, 369–390 (1990).

70. G. H. Brimhall, *et al.*, Deformational mass transport and invasive processes in soil evolution. *Science* **255**, 695–702 (1992).

71. N. D. Sheldon, N. J. Tabor, Quantitative paleoenvironmental and paleoclimatic reconstruction using paleosols. *Earth-Science Reviews* **95**, 1–52 (2009).

72. J. Palandri, Y. Kharaka, A Compilation of Rate Parameters of Water-Mineral Interaction Kinetics for Application to Geochemical Modeling. **1068**, 71 (2004).

73. D. Wolff-Boenisch, S. R. Gislason, E. H. Oelkers, C. V. Putnis, The dissolution rates of natural glasses as a function of their composition at pH 4 and 10.6, and temperatures from 25 to 74°C. *Geochimica et Cosmochimica Acta* **68**, 4843–4858 (2004).

74. S. R. Gislason, E. H. Oelkers, Mechanism, rates, and consequences of basaltic glass dissolution: II. An experimental study of the dissolution rates of basaltic glass as a function of pH and temperature. *Geochimica et Cosmochimica Acta* **67**, 3817–3832 (2003).

75. S. H. Baek, *et al.*, Impact of Climate on the Global Capacity for Enhanced Rock Weathering on Croplands. *Earth's Future* **11**, e2023EF003698 (2023).

76. How surface roughness scaling can mislead enhanced weathering predictions – CarbonPlan. Available at: https://carbonplan.org/research/modeling-bytes-02-roughness [Accessed 9 August 2026].

Supplementary Tables and Figures:

Table 1. Coefficient of variance (CV) of baseline pH and base saturation across applied fields.

Site Name	Baseline pH CV	Baseline Base Saturation (Ca + Mg) (%) CV
A	0.0496	0.098
B	0.0449	0.0856
C	0.0441	0.0689
D	0.0721	0.1035
E	0.0657	0.1501
F	0.0498	0.0928
G	0.0956	0.2592
H	0.1219	0.2762
I	0.0647	0.1572
J	0.0319	0.048
K	0.0464	0.0746
L	0.0502	0.0732
M	0.1025	0.158
N	0.043	0.0495
O	0.0508	0.0981
P	0.0727	0.2449
Q	0.0901	0.1802
R	0.053	0.1517
S	0.0562	0.1886
T	0.0598	0.1293
U	0.0409	0.1611
V	0.0488	0.0894
W	0.0409	0.0915
X	0.0364	0.0861
Cross-Field Variance	**0.00051**	**0.00413**

Table 2. Coefficient of variation (CV) of baseline pH and base saturation across control fields.

Site Name	Baseline pH CV	Baseline Base Saturation (Ca + Mg) (%) CV
A	0.0971	0.2861
B	0.1176	0.1759
C	0.0607	0.1264
D	0.0709	0.1411
E	0.0975	0.2904
F	0.0736	0.1397
G	0.0783	0.1565
H	0.1315	0.3268
I	0.0574	0.1119
J	0.1079	0.2711
K	0.1645	0.2551
L	0.0668	0.0789
M	0.0584	0.1305
N	0.0807	0.1610
O	0.0964	0.2313
P	0.0532	0.1479
Q	0.0736	0.1117
R	0.1178	0.3031
S	0.0606	0.1758
T	0.1039	0.1471
U	0.0317	0.0761
V	0.0438	0.1633
W	0.0829	0.2125
X	0.08579	0.1223
Cross-Field Variance	**0.00091**	**0.00536**

Table 3. Comparison of published CDR estimates from reactive transport models.

Study	Time	CDR ($t\ CO_2\ ha^{-1}$)	Feedstock Diameter	Study Design
Vienne et al. 2022 (15)	1 year	1.83	250 μm	PHREEQC: 1 m mesocosm, 50 t ha^{-1} basalt
Tu et al. 2026 (59)	1 year	0-2	N/A	Scaled model based on regional precipitation and temperature regimes
Goll et al. 2021 (60)	1 year	0.45	20 μm	ORCHIDEE-CP: 50t/ha basalt, analysis on global hinterlands
Baek et al. 2023 (75)	1 year	1.14-1.16	100 μm	SCEPTER: basalt, 10t/ha application, global analysis but data is specific to the US southeast
Khalidy et al. 2024 (61)	500 days	8.3	N/A	Geochemists Workbench: 60 cm soil column, 50t ha^{-1} basalt
Kelland et al. 2020 (62)	2 years	3	1,250 μm	PHREEQC: 250 mm deep soil column, 100 t ha^{-1} basalt
Lewis et al. 2021 (63)	15 years	1.3-8.5	267-1767 μm	PHREEQC model from Kelland et al. 2020 (61), 50 t ha^{-1} basalt

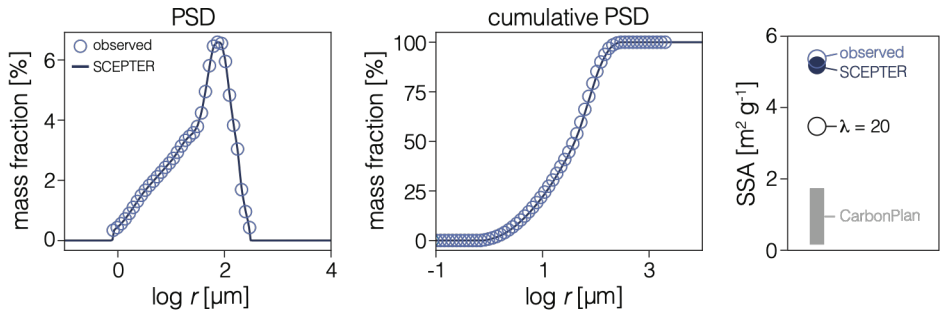

Figure 1. Particle size distribution (PSD) and specific surface area (SSA) of applied basalt feedstock. The p80 of the basalt is 89.92 uM, and the specific surface area is approximately 5.24 m^2/g. SCEPTER-generated surface roughness values from Baek et al. (2023) are shown in blue, approximated specific surface area using a surface roughness of $\lambda = 20$, and the surface area approximated by (76) is shown for comparison.

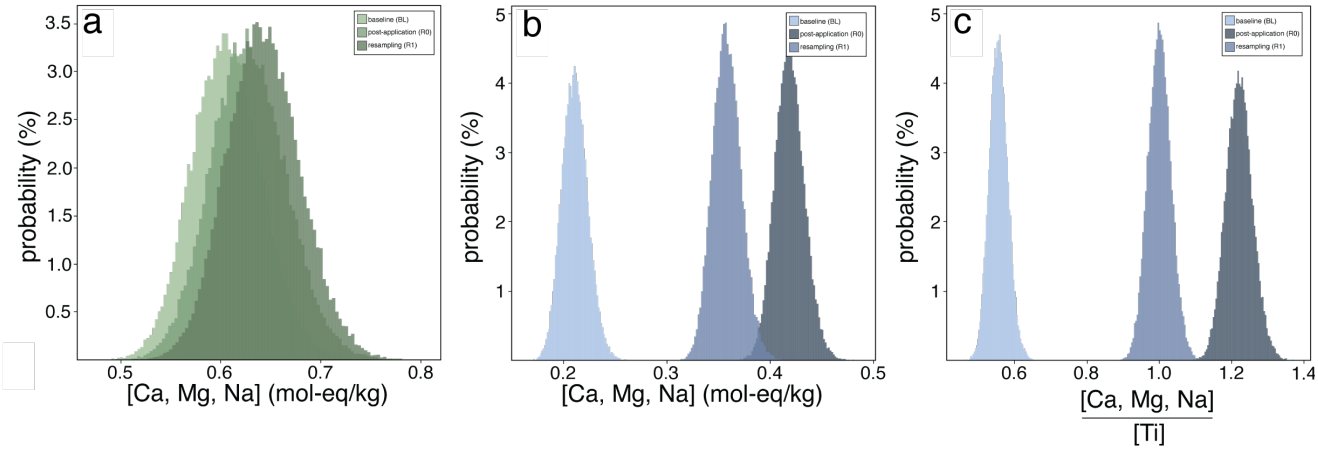

Figure 2. Bootstrapped population cation and Ti-corrected cation concentration for control and basalt-amended fields. All samples for each timepoint were calculated for concentration, then bootstrapped with 50,000 simulations. The sampling timepoints (BL, PA, RS) for basalt are shown in blue, and control is shown in green. a) Molar-equivalent cation concentrations for control fields at BL, PA, and RS timepoints. b) Molar-equivalent cation concentrations for basalt-amended fields for BL, PA, and RS timepoints. c) Ti-corrected molar-equivalent cation concentrations for basalt-amended fields for BL, PA, and RS timepoints.

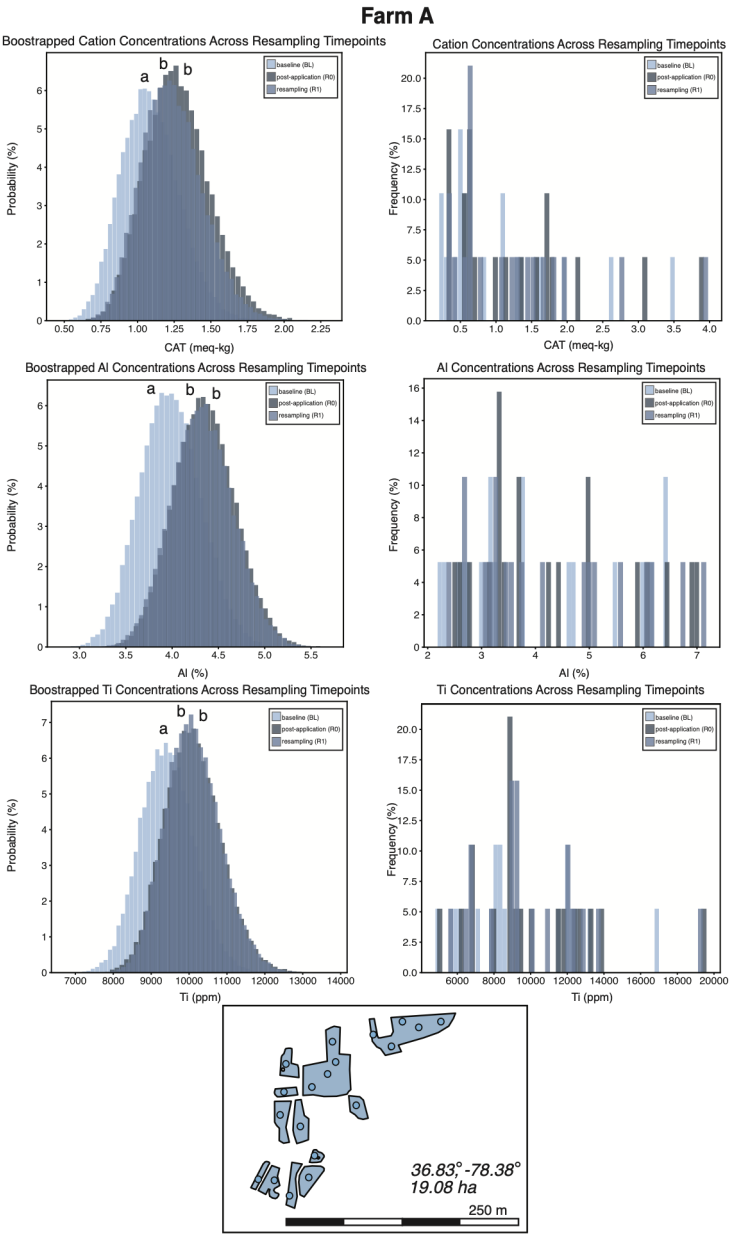

Figure 3. Bootstrapped Concentrations, Resampling Histograms, and Map of Fields and Point Distributions for Farm A. Bootstraps used a total of 50,000 simulations to simulate a given mean dissolution percentage on the x-axis, with relative probabilities (%) for outcome on the y-axis. Histograms show the relative frequency (%) on the y-axis, against the given concentration value on the x-axis for major cations [Ca^{2+}, Mg^{2+}, Na^{+}], Al, and Ti, with units given as mol-eq kg^{-1}, %, and ppm, respectively. Paired t-tests were conducted on unbootstrapped populations, with significance displayed on bootstrapped plots for clarity. Maps of field and sampling distributions are also shown, with anonymized latitudes and longitudes, as well as total hectares included. The scale of the map is given in meters, with a single rectangle being equivalent to 250 m.

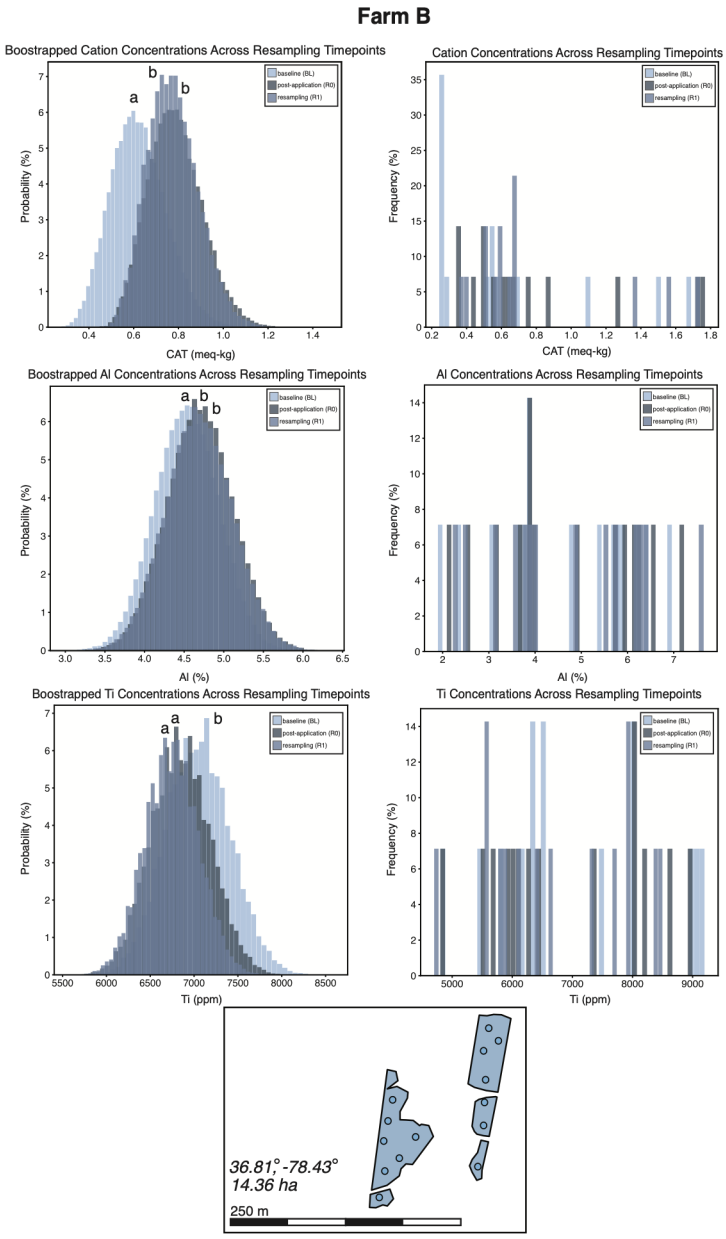

Figure 4. Bootstrapped Concentrations, Resampling Histograms, and Map of Fields and Point Distributions for Farm B. Bootstraps used a total of 50,000 simulations to simulate a given mean dissolution percentage on the x-axis, with relative probabilities (%) for outcome on the y-axis. Histograms show the relative frequency (%) on the y-axis, against the given concentration value on the x-axis for major cations [Ca^{2+}, Mg^{2+}, Na^{+}], Al, and Ti, with units given as mol-eq kg^{-1}, %, and ppm, respectively. Paired t-tests were conducted on unbootstrapped populations, with significance displayed on bootstrapped plots for clarity. Maps of field and sampling distributions are also shown, with anonymized latitudes and longitudes, as well as total hectares included. The scale of the map is given in meters, with a single rectangle being equivalent to 250 m.

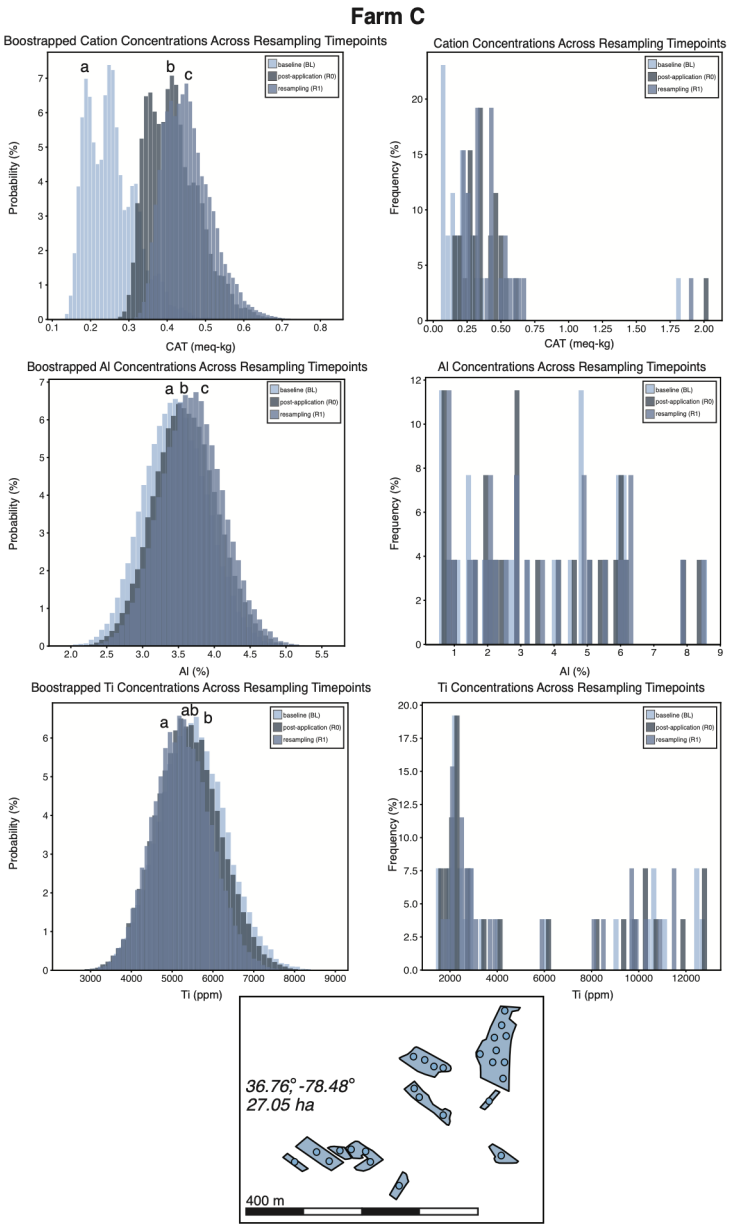

Figure 5. Bootstrapped Concentrations, Resampling Histograms, and Map of Fields and Point Distributions for Farm C. Bootstraps used a total of 50,000 simulations to simulate a given mean dissolution percentage on the x-axis, with relative probabilities (%) for outcome on the y-axis. Histograms show the relative frequency (%) on the y-axis, against the given concentration value on the x-axis for major cations [Ca^{2+}, Mg^{2+}, Na^{+}], Al, and Ti, with units given as mol-eq kg^{-1}, %, and ppm, respectively. Paired t-tests were conducted on unbootstrapped populations, with significance displayed on bootstrapped plots for clarity. Maps of field and sampling distributions are also shown, with anonymized latitudes and longitudes, as well as total hectares included. The scale of the map is given in meters, with a single rectangle being equivalent to 400 m.

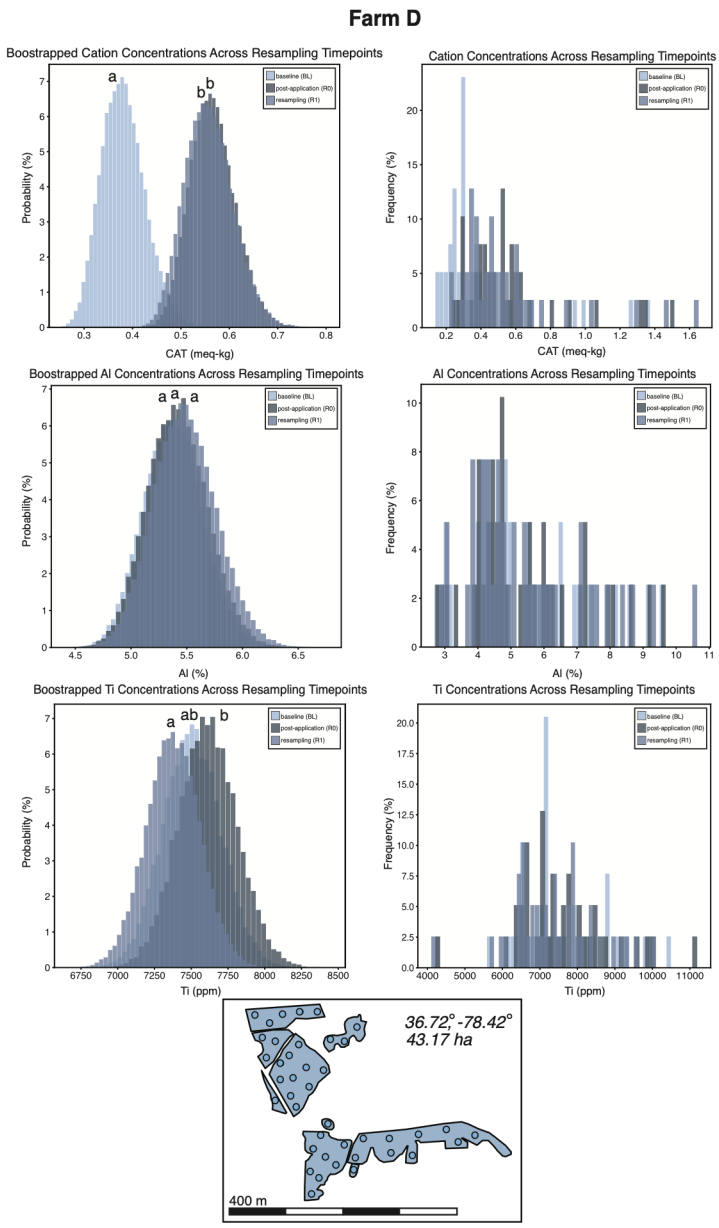

Figure 6. Bootstrapped Concentrations, Resampling Histograms, and Map of Fields and Point Distributions for Farm D. Bootstraps used a total of 50,000 simulations to simulate a given mean dissolution percentage on the x-axis, with relative probabilities (%) for outcome on the y-axis. Histograms show the relative frequency (%) on the y-axis, against the given concentration value on the x-axis for major cations [Ca^{2+}, Mg^{2+}, Na^{+}], Al, and Ti, with units given as mol-eq kg^{-1}, %, and ppm, respectively. Paired t-tests were conducted on unbootstrapped populations, with significance displayed on bootstrapped plots for clarity. Maps of field and sampling distributions are also shown, with anonymized latitudes and longitudes, as well as total hectares included. The scale of the map is given in meters, with a single rectangle being equivalent to 400 m.

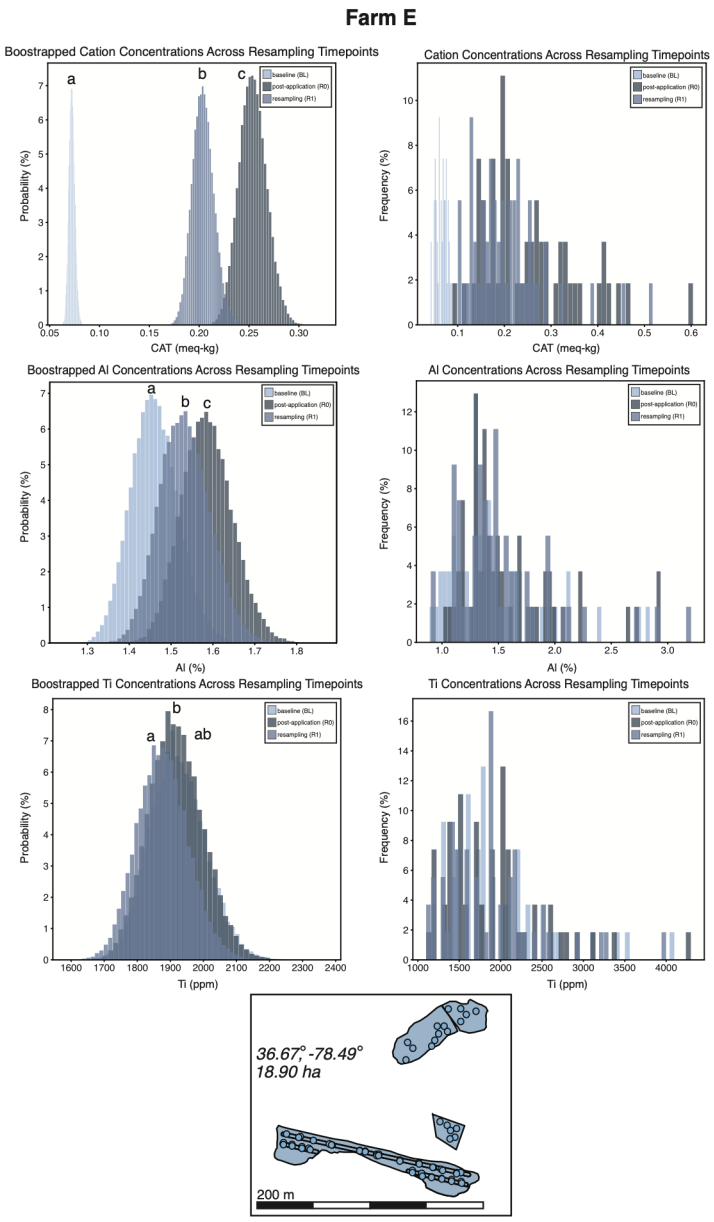

Figure 7. Bootstrapped Concentrations, Resampling Histograms, and Map of Fields and Point Distributions for Farm E. Bootstraps used a total of 50,000 simulations to simulate a given mean dissolution percentage on the x-axis, with relative probabilities (%) for outcome on the y-axis. Histograms show the relative frequency (%) on the y-axis, against the given concentration value on the x-axis for major cations [Ca^{2+}, Mg^{2+}, Na^{+}], Al, and Ti, with units given as mol-eq kg^{-1}, %, and ppm, respectively. Paired t-tests were conducted on unbootstrapped populations, with significance displayed on bootstrapped plots for clarity. Maps of field and sampling distributions are also shown, with anonymized latitudes and longitudes, as well as total hectares included. The scale of the map is given in meters, with a single rectangle being equivalent to 200 m.

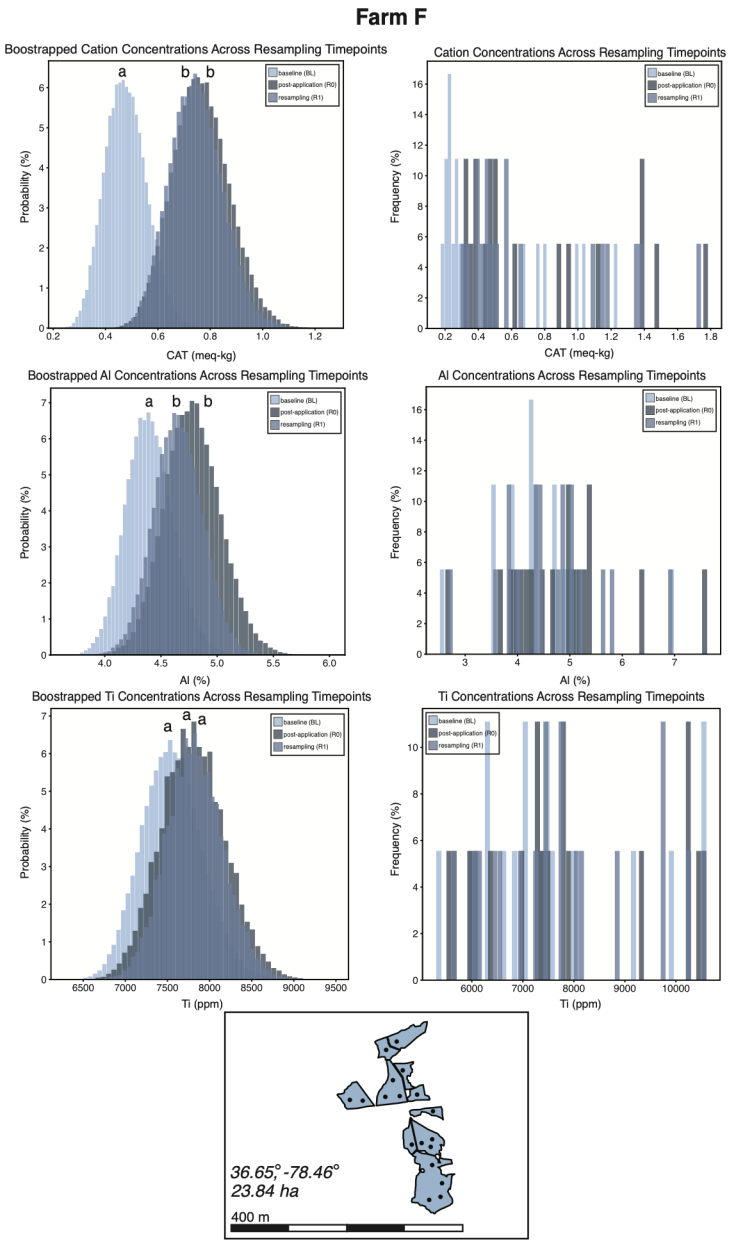

Figure 8. Bootstrapped Concentrations, Resampling Histograms, and Map of Fields and Point Distributions for Farm F. Bootstraps used a total of 50,000 simulations to simulate a given mean dissolution percentage on the x-axis, with relative probabilities (%) for outcome on the y-axis. Histograms show the relative frequency (%) on the y-axis, against the given concentration value on the x-axis for major cations [Ca^{2+}, Mg^{2+}, Na^{+}], Al, and Ti, with units given as mol-eq kg^{-1}, %, and ppm, respectively. Paired t-tests were conducted on unbootstrapped populations, with significance displayed on bootstrapped plots for clarity. Maps of field and sampling distributions are also shown, with anonymized latitudes and longitudes, as well as total hectares included. The scale of the map is given in meters, with a single rectangle being equivalent to 400 m.

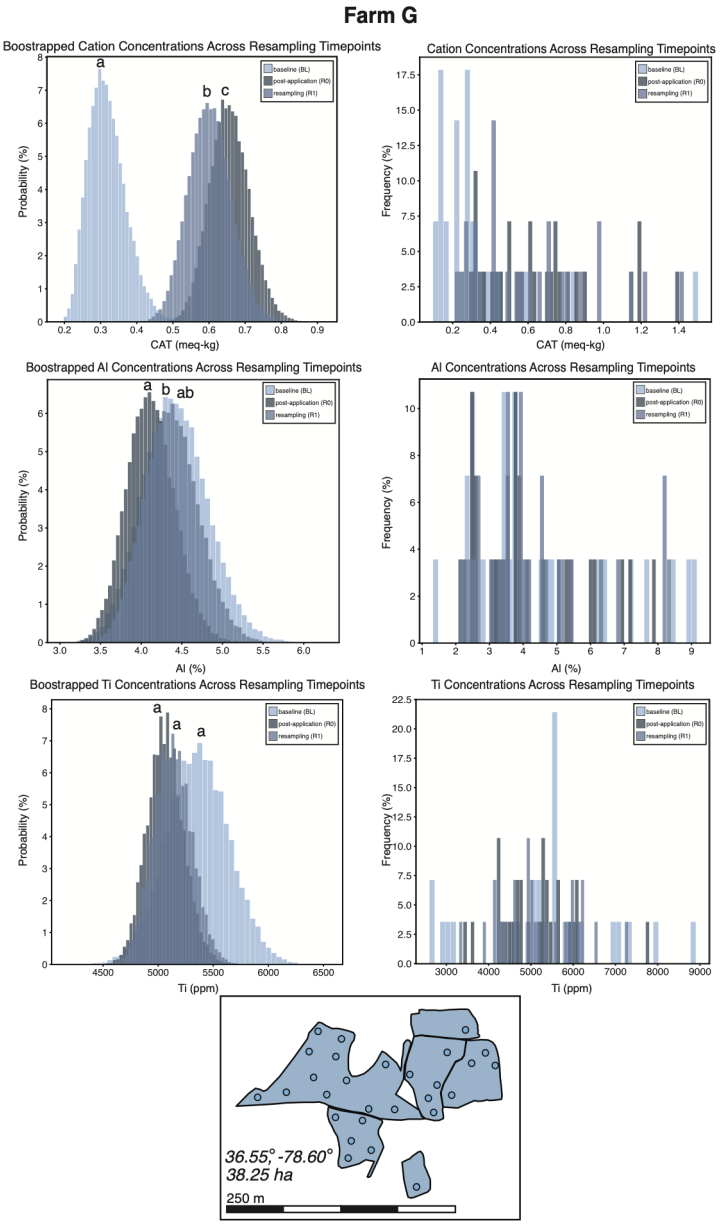

Figure 9. Bootstrapped Concentrations, Resampling Histograms, and Map of Fields and Point Distributions for Farm G. Bootstraps used a total of 50,000 simulations to simulate a given mean dissolution percentage on the x-axis, with relative probabilities (%) for outcome on the y-axis. Histograms show the relative frequency (%) on the y-axis, against the given concentration value on the x-axis for major cations [Ca^{2+}, Mg^{2+}, Na^{+}], Al, and Ti, with units given as mol-eq kg^{-1}, %, and ppm, respectively. Paired t-tests were conducted on unbootstrapped populations, with significance displayed on bootstrapped plots for clarity. Maps of field and sampling distributions are also shown, with anonymized latitudes and longitudes, as well as total hectares included. The scale of the map is given in meters, with a single rectangle being equivalent to 250 m.

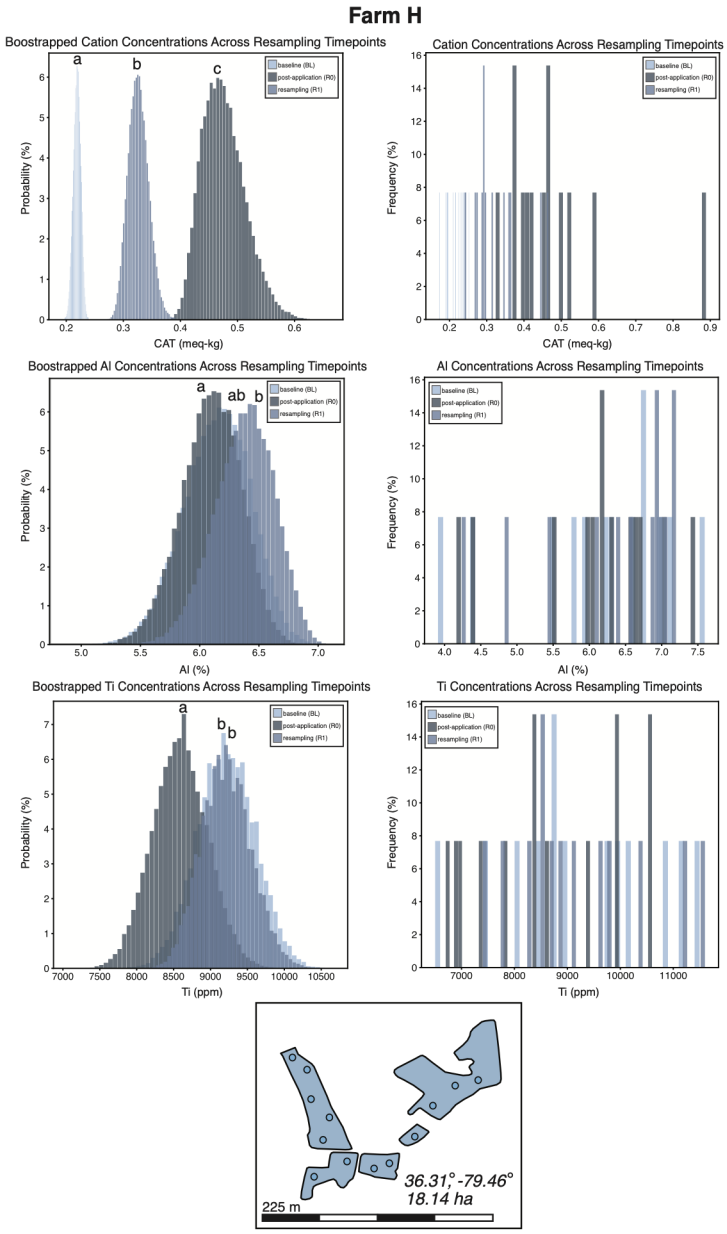

Figure 10. Bootstrapped Concentrations, Resampling Histograms, and Map of Fields and Point Distributions for Farm H. Bootstraps used a total of 50,000 simulations to simulate a given mean dissolution percentage on the x-axis, with relative probabilities (%) for outcome on the y-axis. Histograms show the relative frequency (%) on the y-axis, against the given concentration value on the x-axis for major cations [Ca^{2+}, Mg^{2+}, Na^{+}], Al, and Ti, with units given as mol-eq kg^{-1}, %, and ppm, respectively. Paired t-tests were conducted on unbootstrapped populations, with significance displayed on bootstrapped plots for clarity. Maps of field and sampling distributions are also shown, with anonymized latitudes and longitudes, as well as total hectares included. The scale of the map is given in meters, with a single rectangle being equivalent to 225 m.

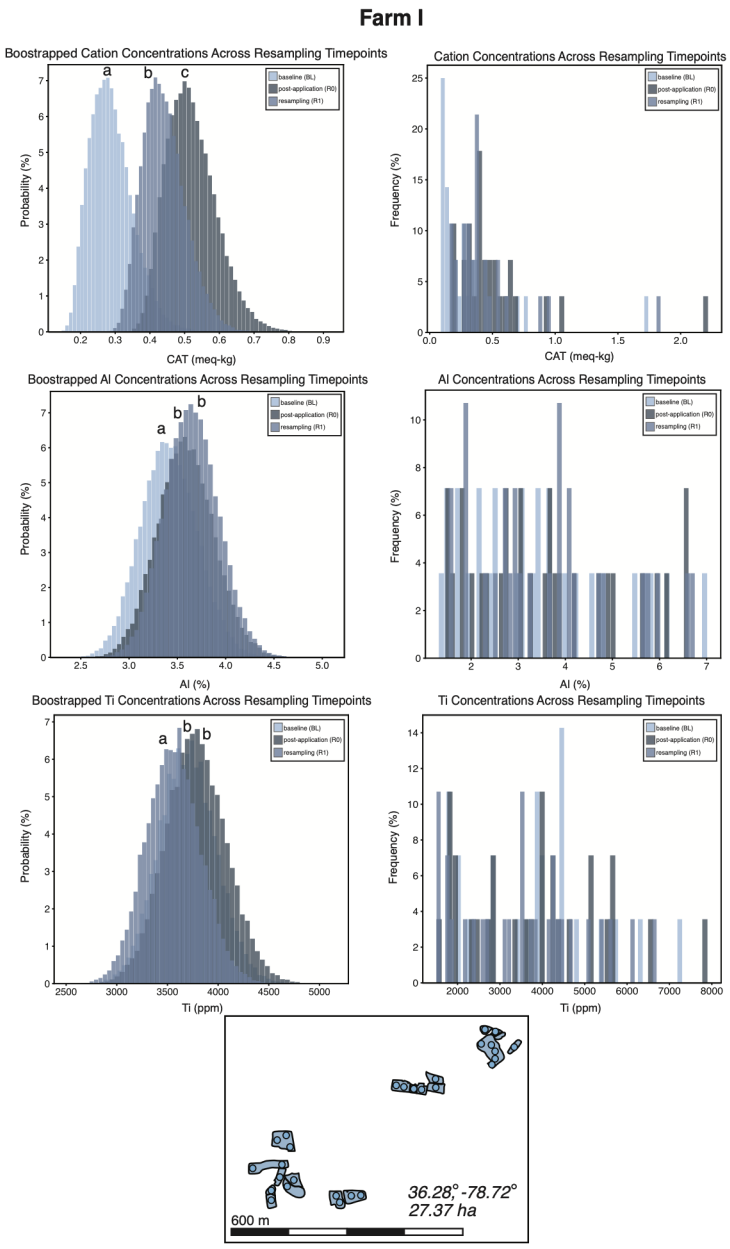

Figure 11. Bootstrapped Concentrations, Resampling Histograms, and Map of Fields and Point Distributions for Farm I. Bootstraps used a total of 50,000 simulations to simulate a given mean dissolution percentage on the x-axis, with relative probabilities (%) for outcome on the y-axis. Histograms show the relative frequency (%) on the y-axis, against the given concentration value on the x-axis for major cations [Ca^{2+}, Mg^{2+}, Na^{+}], Al, and Ti, with units given as mol-eq kg^{-1}, %, and ppm, respectively. Paired t-tests were conducted on unbootstrapped populations, with significance displayed on bootstrapped plots for clarity. Maps of field and sampling distributions are also shown, with anonymized latitudes and longitudes, as well as total hectares included. The scale of the map is given in meters, with a single rectangle being equivalent to 600 m.

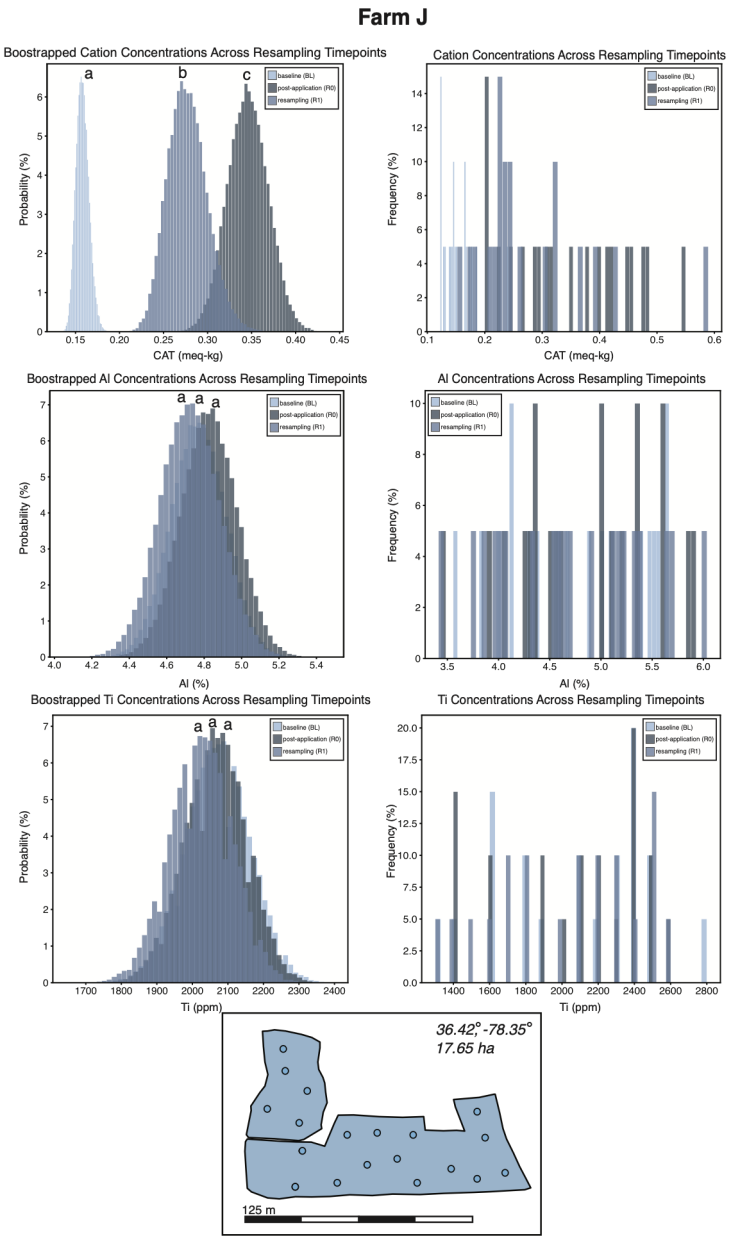

Figure 12. Bootstrapped Concentrations, Resampling Histograms, and Map of Fields and Point Distributions for Farm J. Bootstraps used a total of 50,000 simulations to simulate a given mean dissolution percentage on the x-axis, with relative probabilities (%) for outcome on the y-axis. Histograms show the relative frequency (%) on the y-axis, against the given concentration value on the x-axis for major cations [Ca^{2+}, Mg^{2+}, Na^{+}], Al, and Ti, with units given as mol-eq kg^{-1}, %, and ppm, respectively. Paired t-tests were conducted on unbootstrapped populations, with significance displayed on bootstrapped plots for clarity. Maps of field and sampling distributions are also shown, with anonymized latitudes and longitudes, as well as total hectares included. The scale of the map is given in meters, with a single rectangle being equivalent to 125 m.

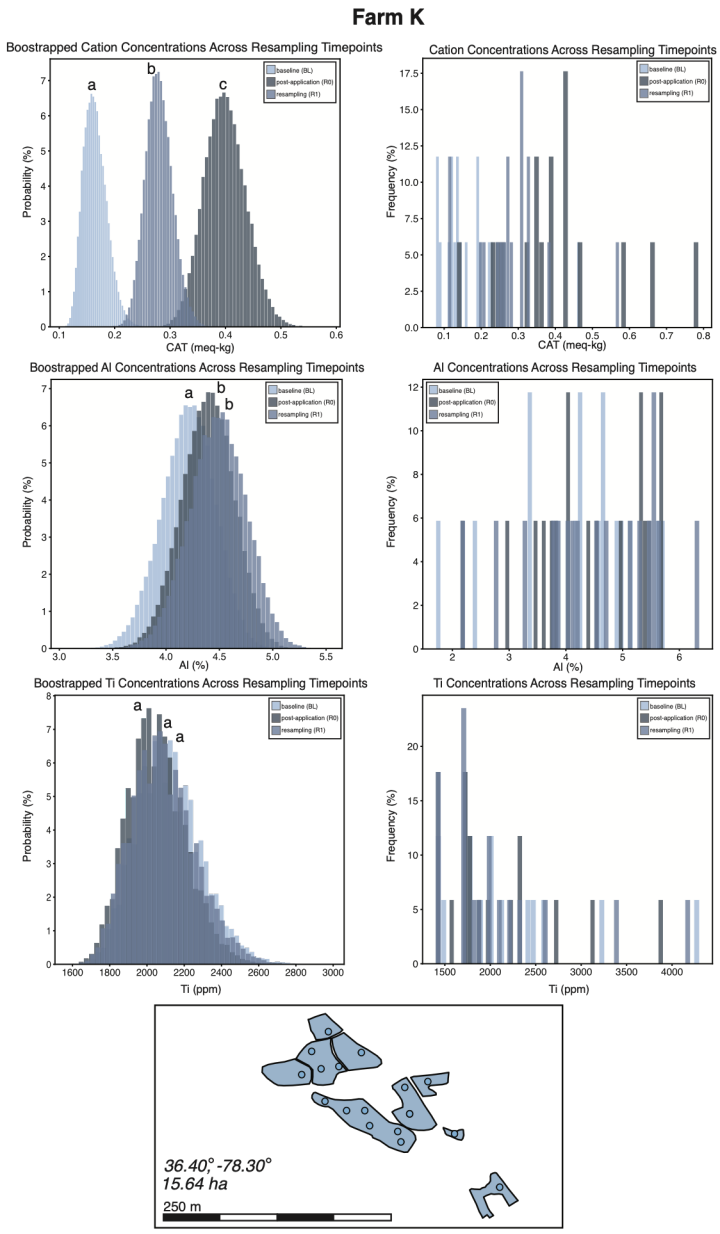

Figure 13. Bootstrapped Concentrations, Resampling Histograms, and Map of Fields and Point Distributions for Farm K. Bootstraps used a total of 50,000 simulations to simulate a given mean dissolution percentage on the x-axis, with relative probabilities (%) for outcome on the y-axis. Histograms show the relative frequency (%) on the y-axis, against the given concentration value on the x-axis for major cations [Ca^{2+}, Mg^{2+}, Na^{+}], Al, and Ti, with units given as mol-eq kg^{-1}, %, and ppm, respectively. Paired t-tests were conducted on unbootstrapped populations, with significance displayed on bootstrapped plots for clarity. Maps of field and sampling distributions are also shown, with anonymized latitudes and longitudes, as well as total hectares included. The scale of the map is given in meters, with a single rectangle being equivalent to 250 m.

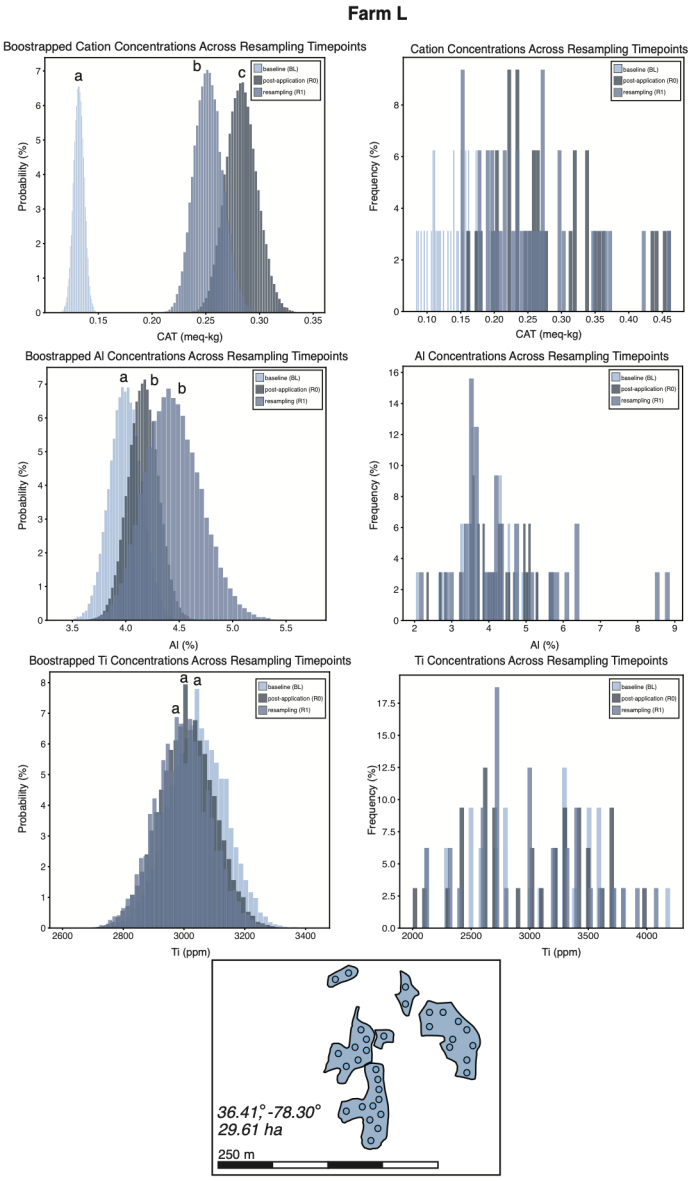

Figure 14. Bootstrapped Concentrations, Resampling Histograms, and Map of Fields and Point Distributions for Farm L. Bootstraps used a total of 50,000 simulations to simulate a given mean dissolution percentage on the x-axis, with relative probabilities (%) for outcome on the y-axis. Histograms show the relative frequency (%) on the y-axis, against the given concentration value on the x-axis for major cations [Ca^{2+}, Mg^{2+}, Na^{+}], Al, and Ti, with units given as mol-eq kg^{-1}, %, and ppm, respectively. Paired t-tests were conducted on unbootstrapped populations, with significance displayed on bootstrapped plots for clarity. Maps of field and sampling distributions are also shown, with anonymized latitudes and longitudes, as well as total hectares included. The scale of the map is given in meters, with a single rectangle being equivalent to 250 m.

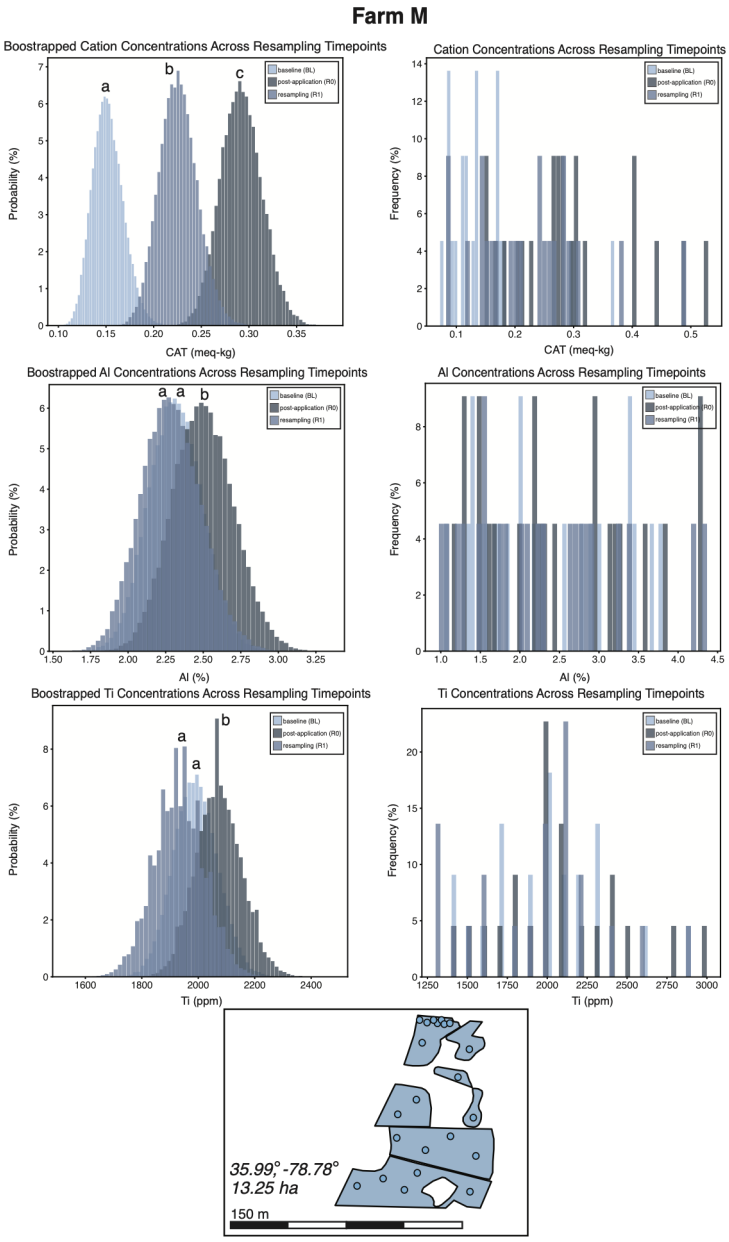

Figure 15. Bootstrapped Concentrations, Resampling Histograms, and Map of Fields and Point Distributions for Farm M. Bootstraps used a total of 50,000 simulations to simulate a given mean dissolution percentage on the x-axis, with relative probabilities (%) for outcome on the y-axis. Histograms show the relative frequency (%) on the y-axis, against the given concentration value on the x-axis for major cations [Ca^{2+}, Mg^{2+}, Na^{+}], Al, and Ti, with units given as mol-eq kg^{-1}, %, and ppm, respectively. Paired t-tests were conducted on unbootstrapped populations, with significance displayed on bootstrapped plots for clarity. Maps of field and sampling distributions are also shown, with anonymized latitudes and longitudes, as well as total hectares included. The scale of the map is given in meters, with a single rectangle being equivalent to 150 m.

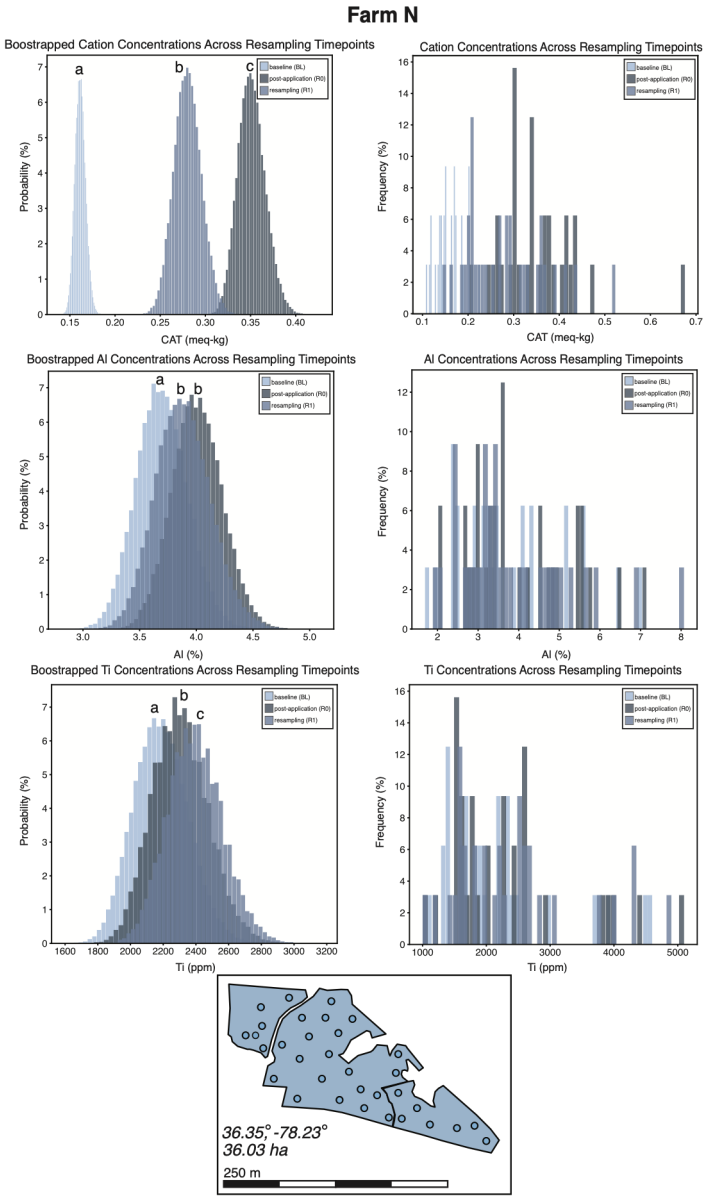

Figure 16. Bootstrapped Concentrations, Resampling Histograms, and Map of Fields and Point Distributions for Farm N. Bootstraps used a total of 50,000 simulations to simulate a given mean dissolution percentage on the x-axis, with relative probabilities (%) for outcome on the y-axis. Histograms show the relative frequency (%) on the y-axis, against the given concentration value on the x-axis for major cations [Ca^{2+}, Mg^{2+}, Na^{+}], Al, and Ti, with units given as mol-eq kg^{-1}, %, and ppm, respectively. Paired t-tests were conducted on unbootstrapped populations, with significance displayed on bootstrapped plots for clarity. Maps of field and sampling distributions are also shown, with anonymized latitudes and longitudes, as well as total hectares included. The scale of the map is given in meters, with a single rectangle being equivalent to 250 m.

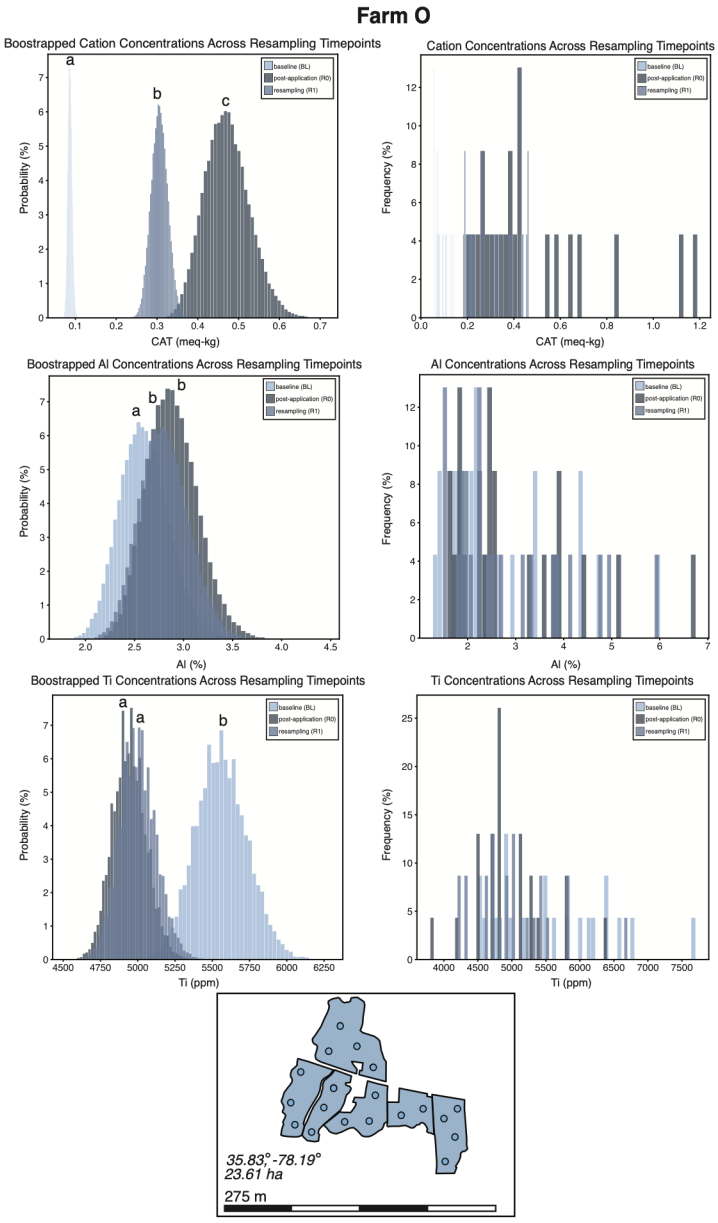

Figure 17. Bootstrapped Concentrations, Resampling Histograms, and Map of Fields and Point Distributions for Farm O. Bootstraps used a total of 50,000 simulations to simulate a given mean dissolution percentage on the x-axis, with relative probabilities (%) for outcome on the y-axis. Histograms show the relative frequency (%) on the y-axis, against the given concentration value on the x-axis for major cations [Ca^{2+}, Mg^{2+}, Na^{+}], Al, and Ti, with units given as mol-eq kg^{-1}, %, and ppm, respectively. Paired t-tests were conducted on unbootstrapped populations, with significance displayed on bootstrapped plots for clarity. Maps of field and sampling distributions are also shown, with anonymized latitudes and longitudes, as well as total hectares included. The scale of the map is given in meters, with a single rectangle being equivalent to 275 m.

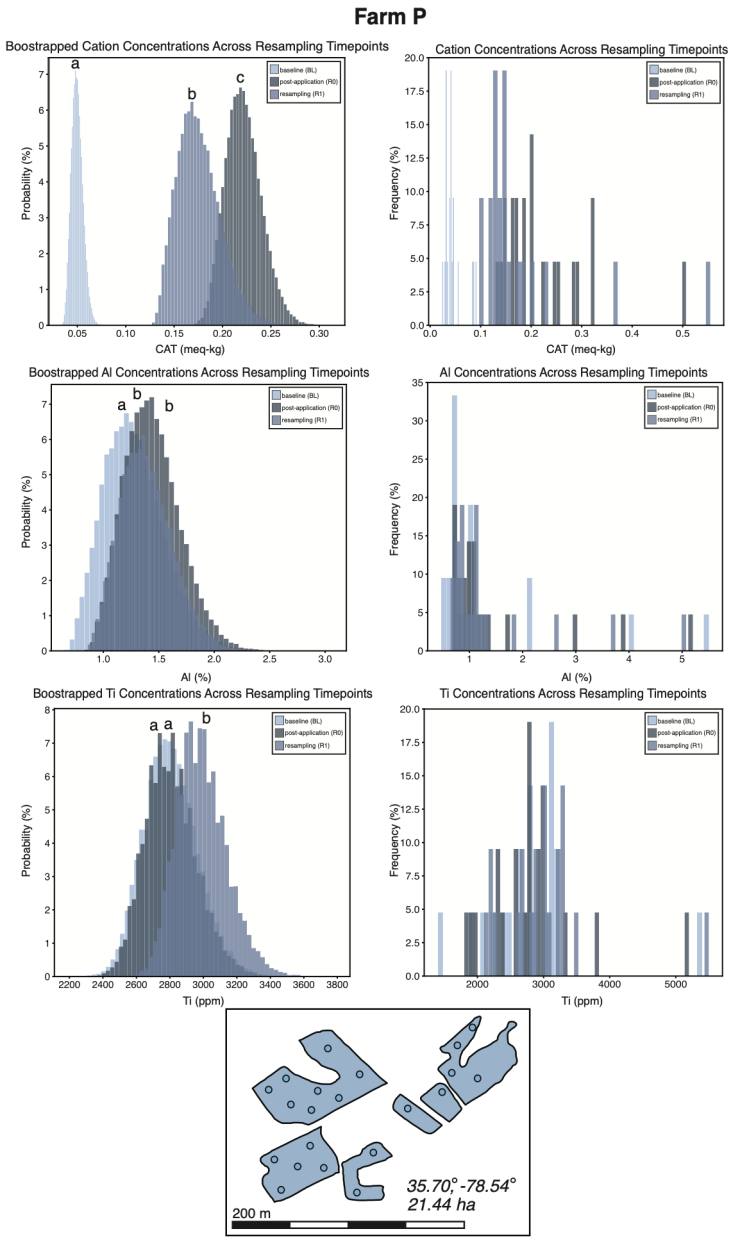

Figure 18. Bootstrapped Concentrations, Resampling Histograms, and Map of Fields and Point Distributions for Farm P. Bootstraps used a total of 50,000 simulations to simulate a given mean dissolution percentage on the x-axis, with relative probabilities (%) for outcome on the y-axis. Histograms show the relative frequency (%) on the y-axis, against the given concentration value on the x-axis for major cations [Ca^{2+}, Mg^{2+}, Na^{+}], Al, and Ti, with units given as mol-eq kg^{-1}, %, and ppm, respectively. Paired t-tests were conducted on unbootstrapped populations, with significance displayed on bootstrapped plots for clarity. Maps of field and sampling distributions are also shown, with anonymized latitudes and longitudes, as well as total hectares included. The scale of the map is given in meters, with a single rectangle being equivalent to 200 m.

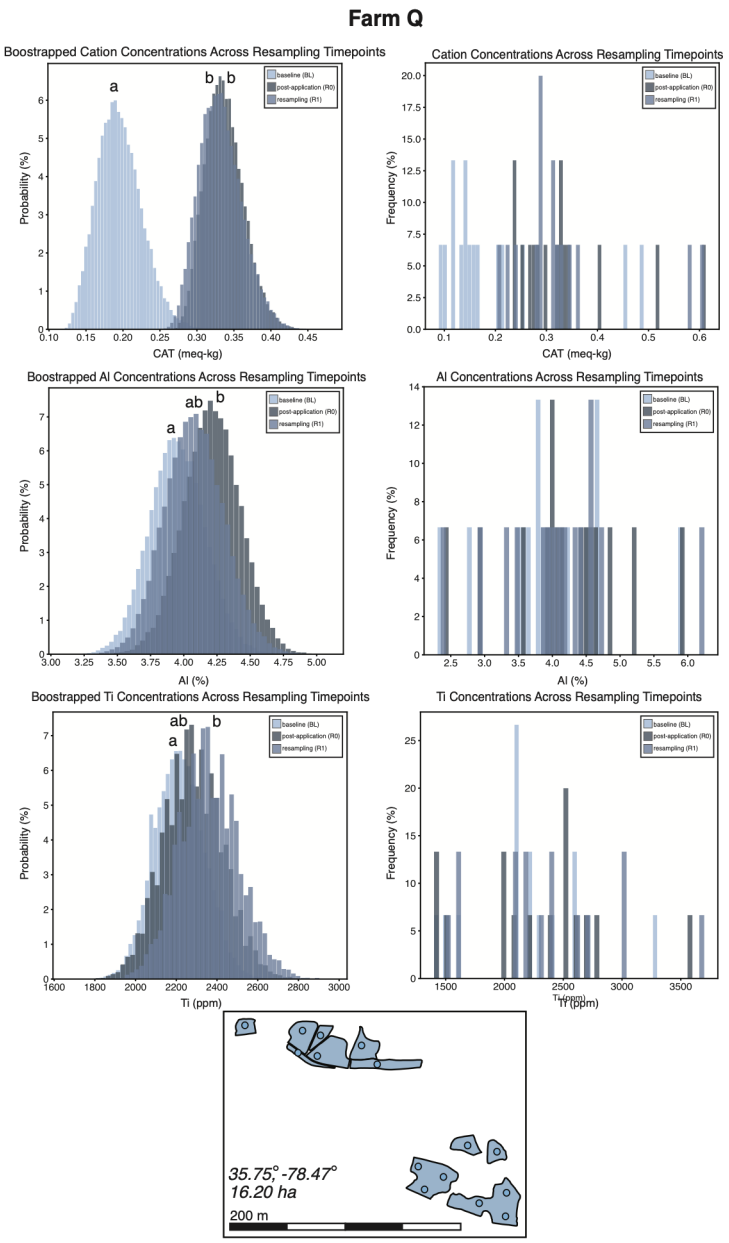

Figure 19. Bootstrapped Concentrations, Resampling Histograms, and Map of Fields and Point Distributions for Farm Q. Bootstraps used a total of 50,000 simulations to simulate a given mean dissolution percentage on the x-axis, with relative probabilities (%) for outcome on the y-axis. Histograms show the relative frequency (%) on the y-axis, against the given concentration value on the x-axis for major cations [Ca^{2+}, Mg^{2+}, Na^{+}], Al, and Ti, with units given as mol-eq kg^{-1}, %, and ppm, respectively. Paired t-tests were conducted on unbootstrapped populations, with significance displayed on bootstrapped plots for clarity. Maps of field and sampling distributions are also shown, with anonymized latitudes and longitudes, as well as total hectares included. The scale of the map is given in meters, with a single rectangle being equivalent to 200 m.

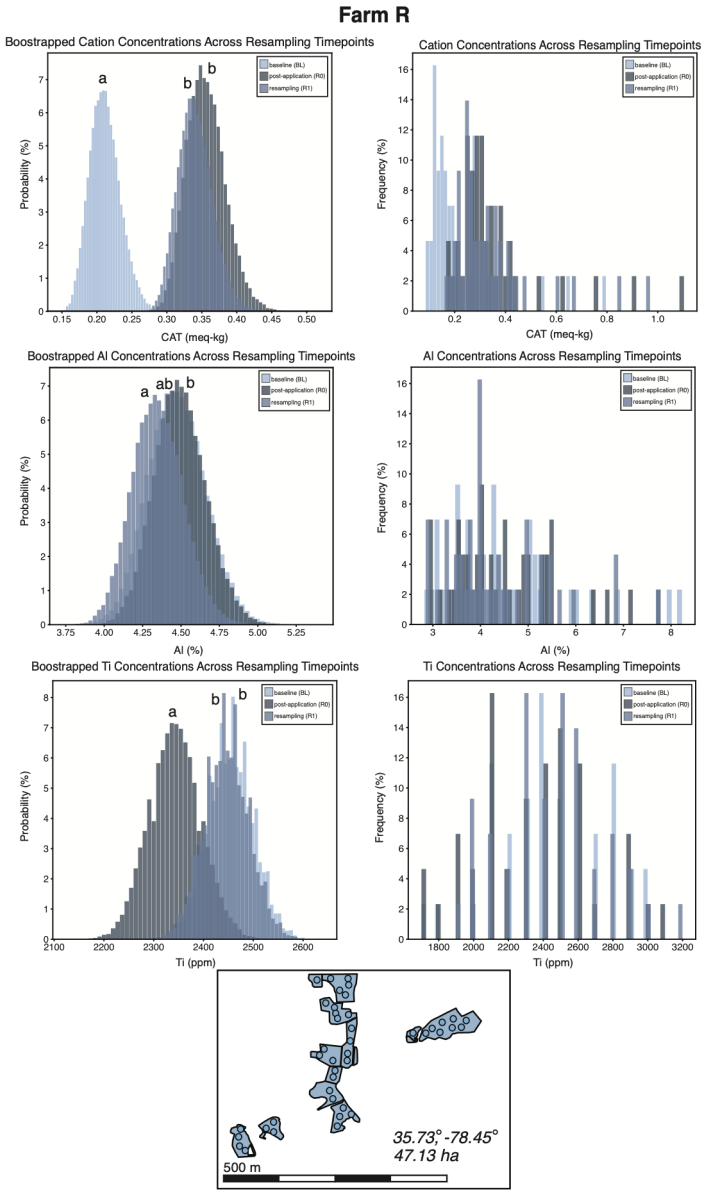

Figure 20. Bootstrapped Concentrations, Resampling Histograms, and Map of Fields and Point Distributions for Farm R. Bootstraps used a total of 50,000 simulations to simulate a given mean dissolution percentage on the x-axis, with relative probabilities (%) for outcome on the y-axis. Histograms show the relative frequency (%) on the y-axis, against the given concentration value on the x-axis for major cations [Ca^{2+}, Mg^{2+}, Na^{+}], Al, and Ti, with units given as mol-eq kg^{-1}, %, and ppm, respectively. Paired t-tests were conducted on unbootstrapped populations, with significance displayed on bootstrapped plots for clarity. Maps of field and sampling distributions are also shown, with anonymized latitudes and longitudes, as well as total hectares included. The scale of the map is given in meters, with a single rectangle being equivalent to 500 m.

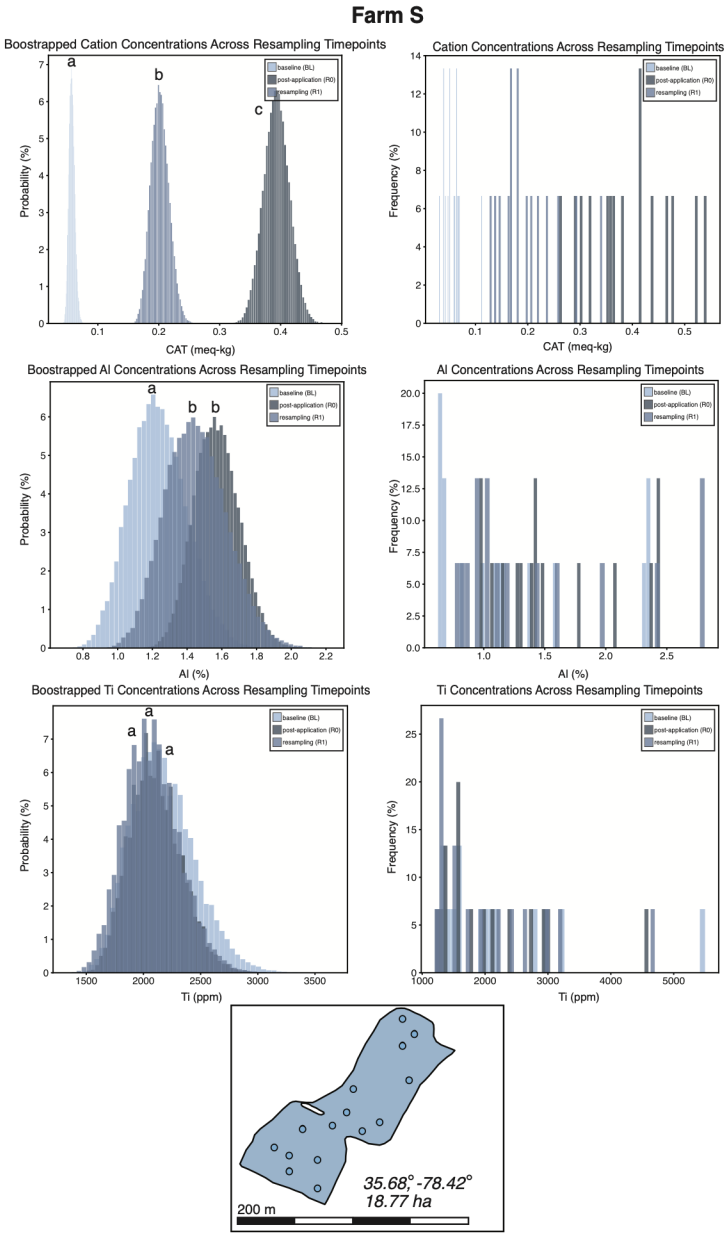

Figure 21. Bootstrapped Concentrations, Resampling Histograms, and Map of Fields and Point Distributions for Farm S. Bootstraps used a total of 50,000 simulations to simulate a given mean dissolution percentage on the x-axis, with relative probabilities (%) for outcome on the y-axis. Histograms show the relative frequency (%) on the y-axis, against the given concentration value on the x-axis for major cations [Ca^{2+}, Mg^{2+}, Na^{+}], Al, and Ti, with units given as mol-eq kg^{-1}, %, and ppm, respectively. Paired t-tests were conducted on unbootstrapped populations, with significance displayed on bootstrapped plots for clarity. Maps of field and sampling distributions are also shown, with anonymized latitudes and longitudes, as well as total hectares included. The scale of the map is given in meters, with a single rectangle being equivalent to 200 m.

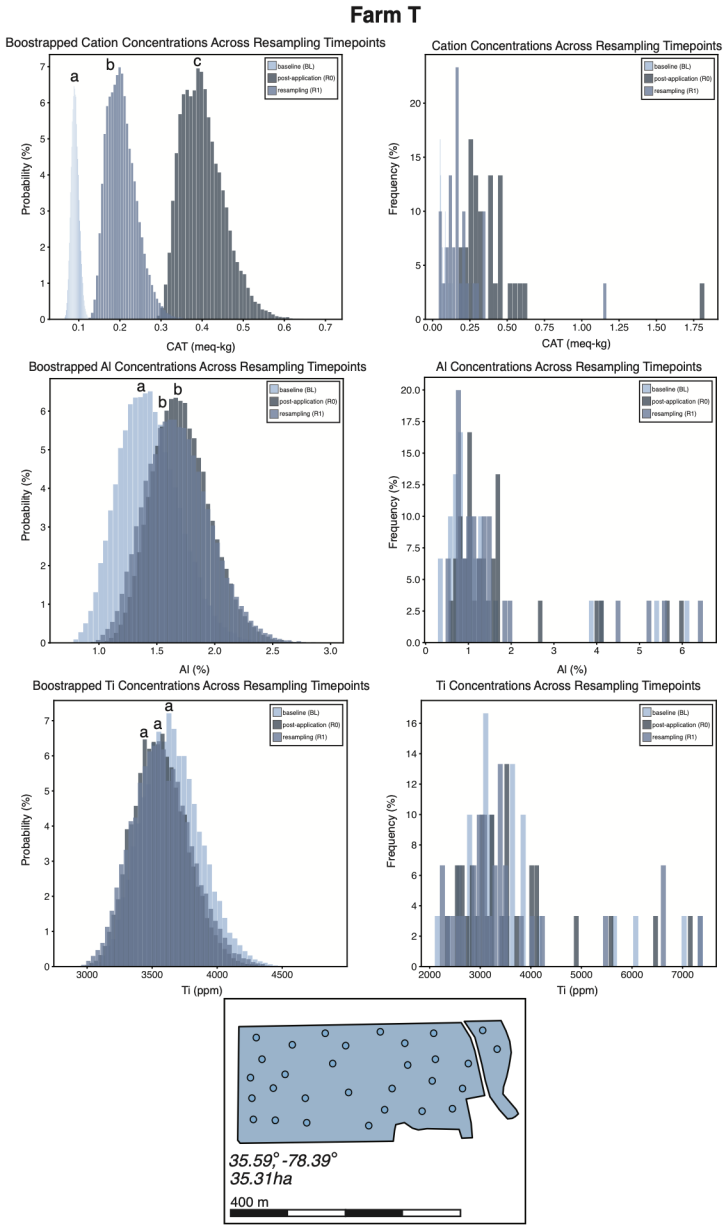

Figure 22. Bootstrapped Concentrations, Resampling Histograms, and Map of Fields and Point Distributions for Farm T. Bootstraps used a total of 50,000 simulations to simulate a given mean dissolution percentage on the x-axis, with relative probabilities (%) for outcome on the y-axis. Histograms show the relative frequency (%) on the y-axis, against the given concentration value on the x-axis for major cations [Ca^{2+}, Mg^{2+}, Na^{+}], Al, and Ti, with units given as mol-eq kg^{-1}, %, and ppm, respectively. Paired t-tests were conducted on unbootstrapped populations, with significance displayed on bootstrapped plots for clarity. Maps of field and sampling distributions are also shown, with anonymized latitudes and longitudes, as well as total hectares included. The scale of the map is given in meters, with a single rectangle being equivalent to 400 m.

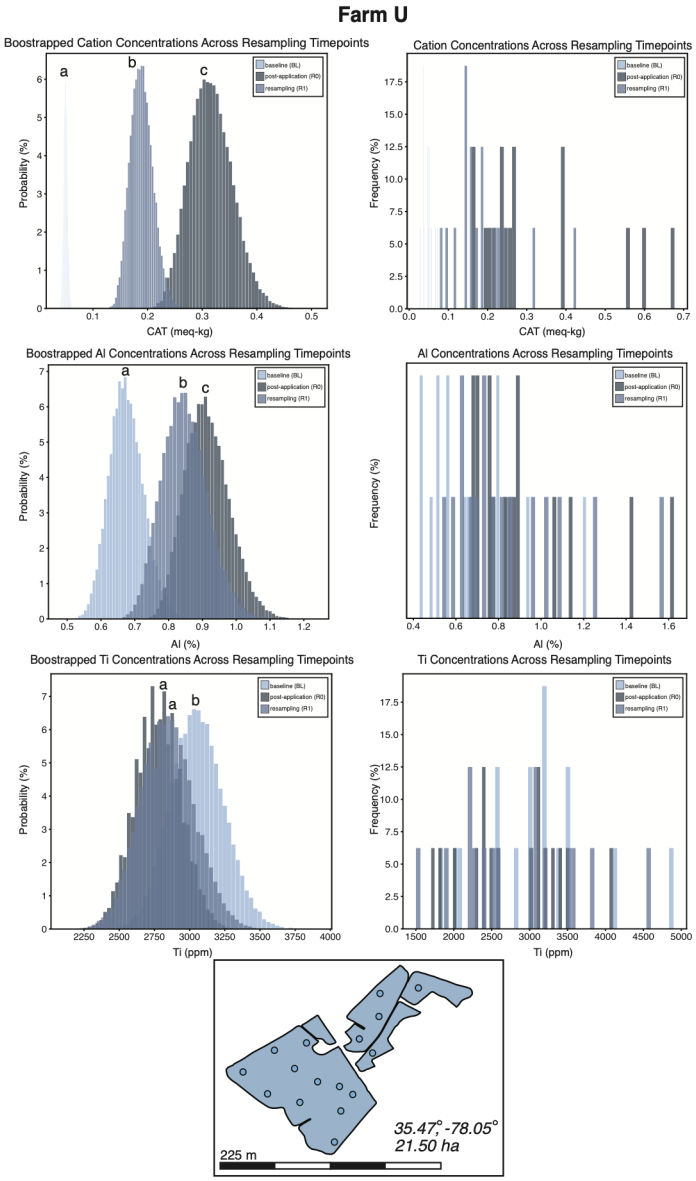

Figure 23. Bootstrapped Concentrations, Resampling Histograms, and Map of Fields and Point Distributions for Farm U. Bootstraps used a total of 50,000 simulations to simulate a given mean dissolution percentage on the x-axis, with relative probabilities (%) for outcome on the y-axis. Histograms show the relative frequency (%) on the y-axis, against the given concentration value on the x-axis for major cations [Ca^{2+}, Mg^{2+}, Na^{+}], Al, and Ti, with units given as mol-eq kg^{-1}, %, and ppm, respectively. Paired t-tests were conducted on unbootstrapped populations, with significance displayed on bootstrapped plots for clarity. Maps of field and sampling distributions are also shown, with anonymized latitudes and longitudes, as well as total hectares included. The scale of the map is given in meters, with a single rectangle being equivalent to 225 m.

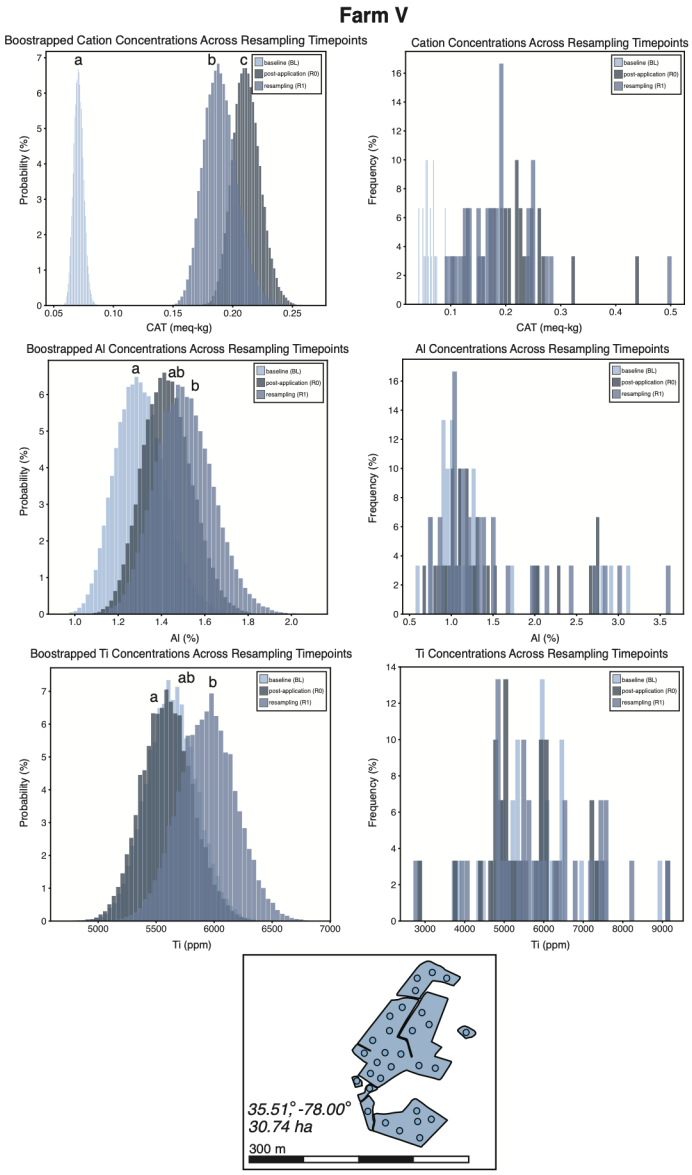

Figure 24. Bootstrapped Concentrations, Resampling Histograms, and Map of Fields and Point Distributions for Farm V. Bootstraps used a total of 50,000 simulations to simulate a given mean dissolution percentage on the x-axis, with relative probabilities (%) for outcome on the y-axis. Histograms show the relative frequency (%) on the y-axis, against the given concentration value on the x-axis for major cations [Ca^{2+}, Mg^{2+}, Na^{+}], Al, and Ti, with units given as mol-eq kg^{-1}, %, and ppm, respectively. Paired t-tests were conducted on unbootstrapped populations, with significance displayed on bootstrapped plots for clarity. Maps of field and sampling distributions are also shown, with anonymized latitudes and longitudes, as well as total hectares included. The scale of the map is given in meters, with a single rectangle being equivalent to 300 m.

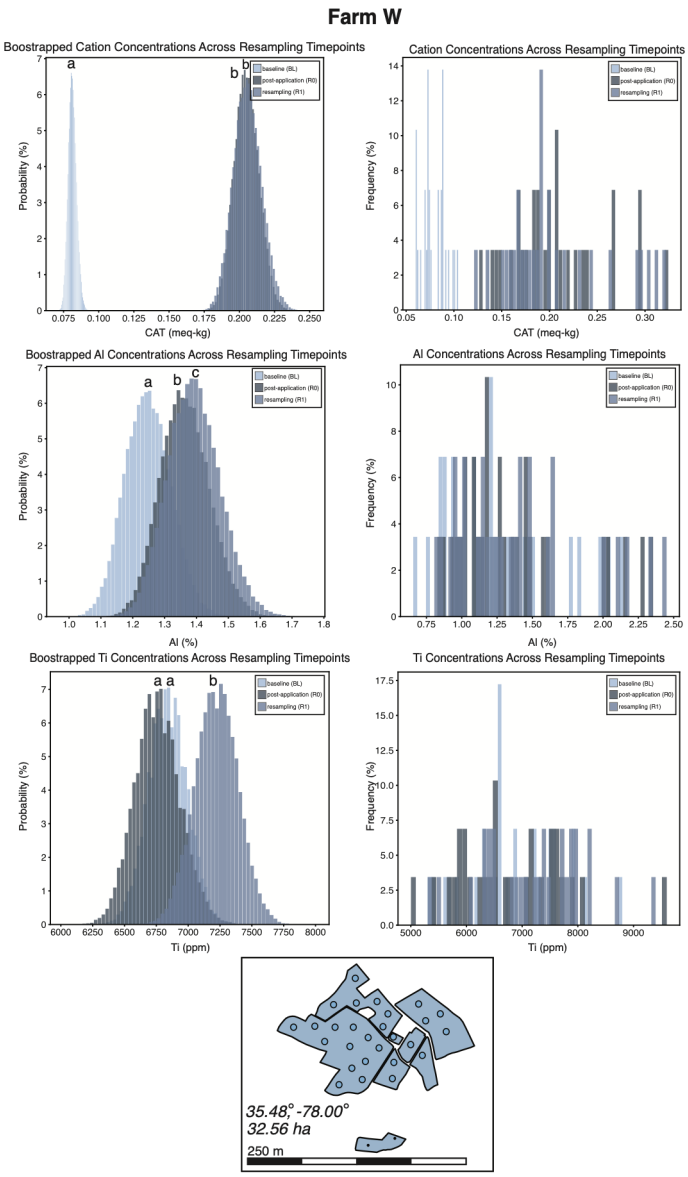

Figure 25. Bootstrapped Concentrations, Resampling Histograms, and Map of Fields and Point Distributions for Farm W. Bootstraps used a total of 50,000 simulations to simulate a given mean dissolution percentage on the x-axis, with relative probabilities (%) for outcome on the y-axis. Histograms show the relative frequency (%) on the y-axis, against the given concentration value on the x-axis for major cations [Ca^{2+}, Mg^{2+}, Na^{+}], Al, and Ti, with units given as mol-eq kg^{-1}, %, and ppm, respectively. Paired t-tests were conducted on unbootstrapped populations, with significance displayed on bootstrapped plots for clarity. Maps of field and sampling distributions are also shown, with anonymized latitudes and longitudes, as well as total hectares included. The scale of the map is given in meters, with a single rectangle being equivalent to 250 m.

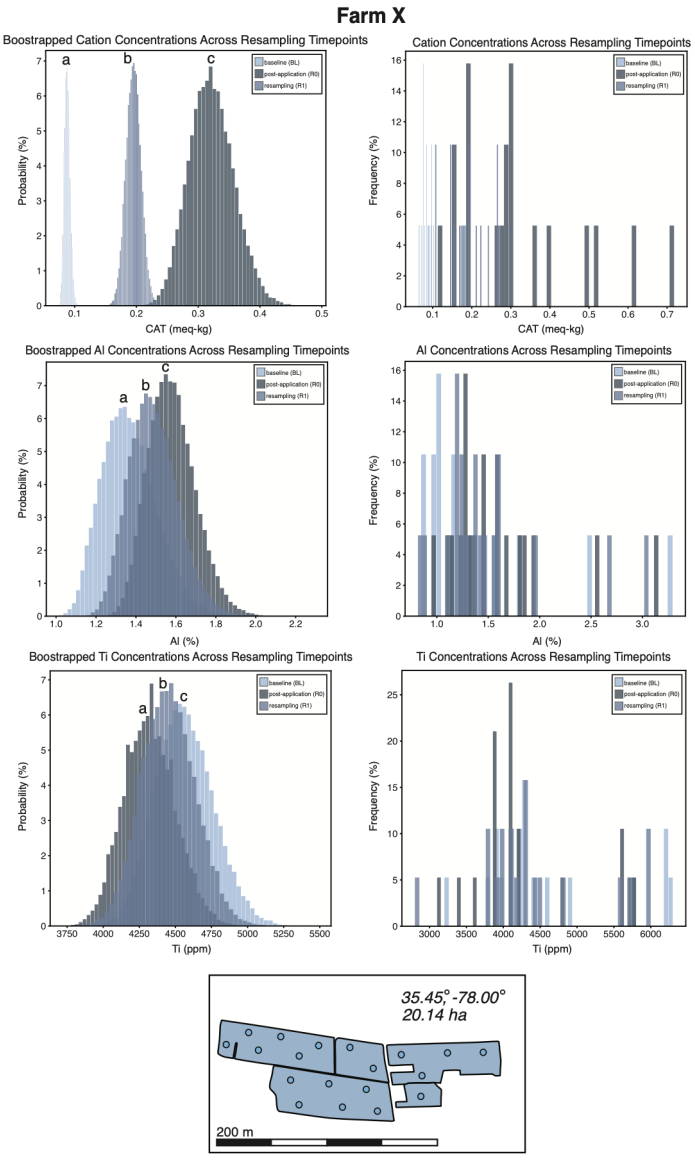

Figure 26. Bootstrapped Concentrations, Resampling Histograms, and Map of Fields and Point Distributions for Farm X. Bootstraps used a total of 50,000 simulations to simulate a given mean dissolution percentage on the x-axis, with relative probabilities (%) for outcome on the y-axis. Histograms show the relative frequency (%) on the y-axis, against the given concentration value on the x-axis for major cations [Ca^{2+}, Mg^{2+}, Na^{+}], Al, and Ti, with units given as mol-eq kg^{-1}, %, and ppm, respectively. Paired t-tests were conducted on unbootstrapped populations, with significance displayed on bootstrapped plots for clarity. Maps of field and sampling distributions are also shown, with anonymized latitudes and longitudes, as well as total hectares included. The scale of the map is given in meters, with a single rectangle being equivalent to 200 m.

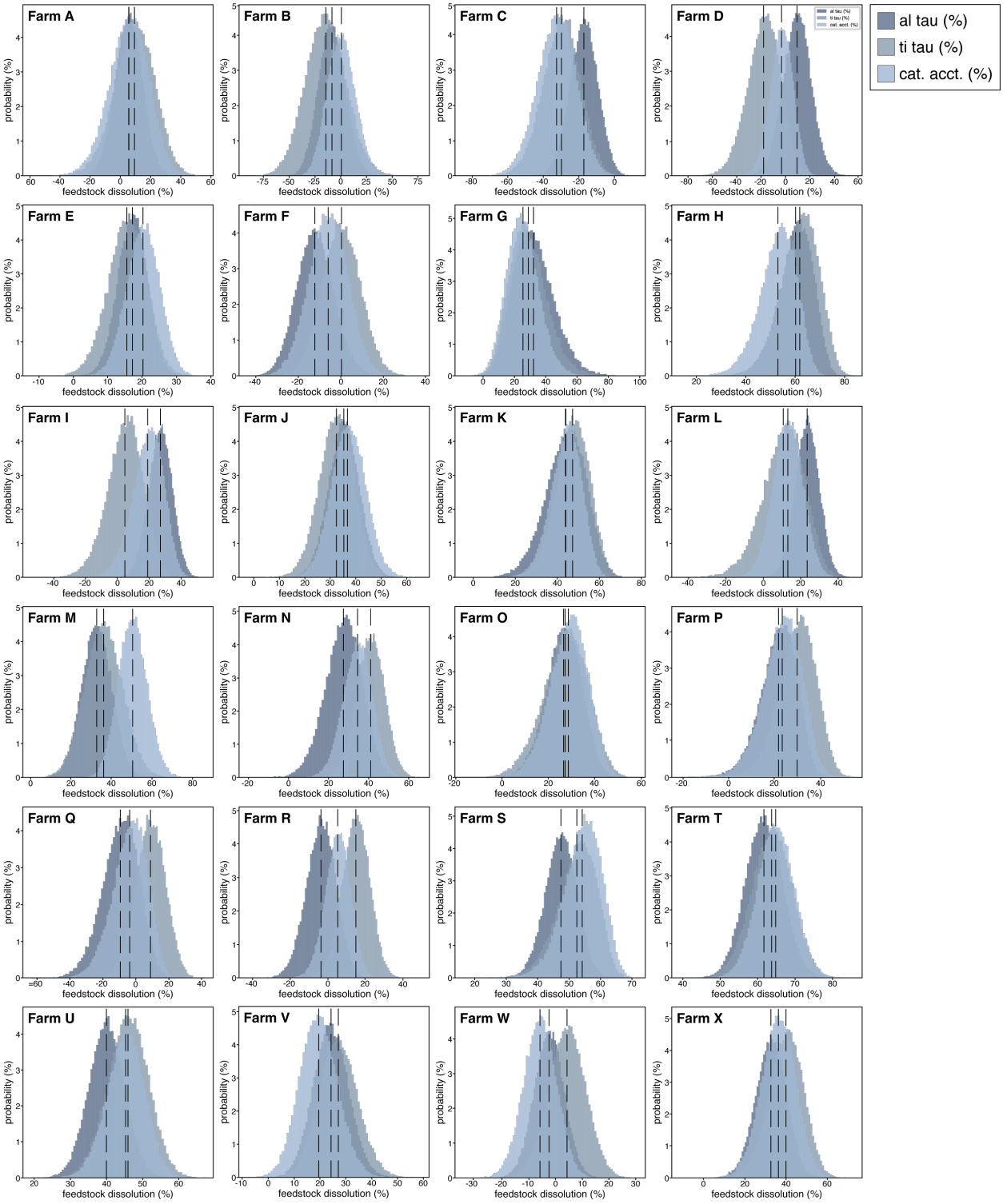

Figure 27. Bootstrapped distribution of cation-based accounting, Al-corrected, and Ti-corrected weathering rate comparison for all presented fields. Each rate population is calculated on a sample-by-sample basis for each field then bootstrapped with replacement (n=50,000). The x-axis shows the comparable dissolution rate, and the y-axis shows the probability of a given mean estimate given the population. Distributions for each method is shown in blue, and means of methods are shown with vertical dashed black lines.

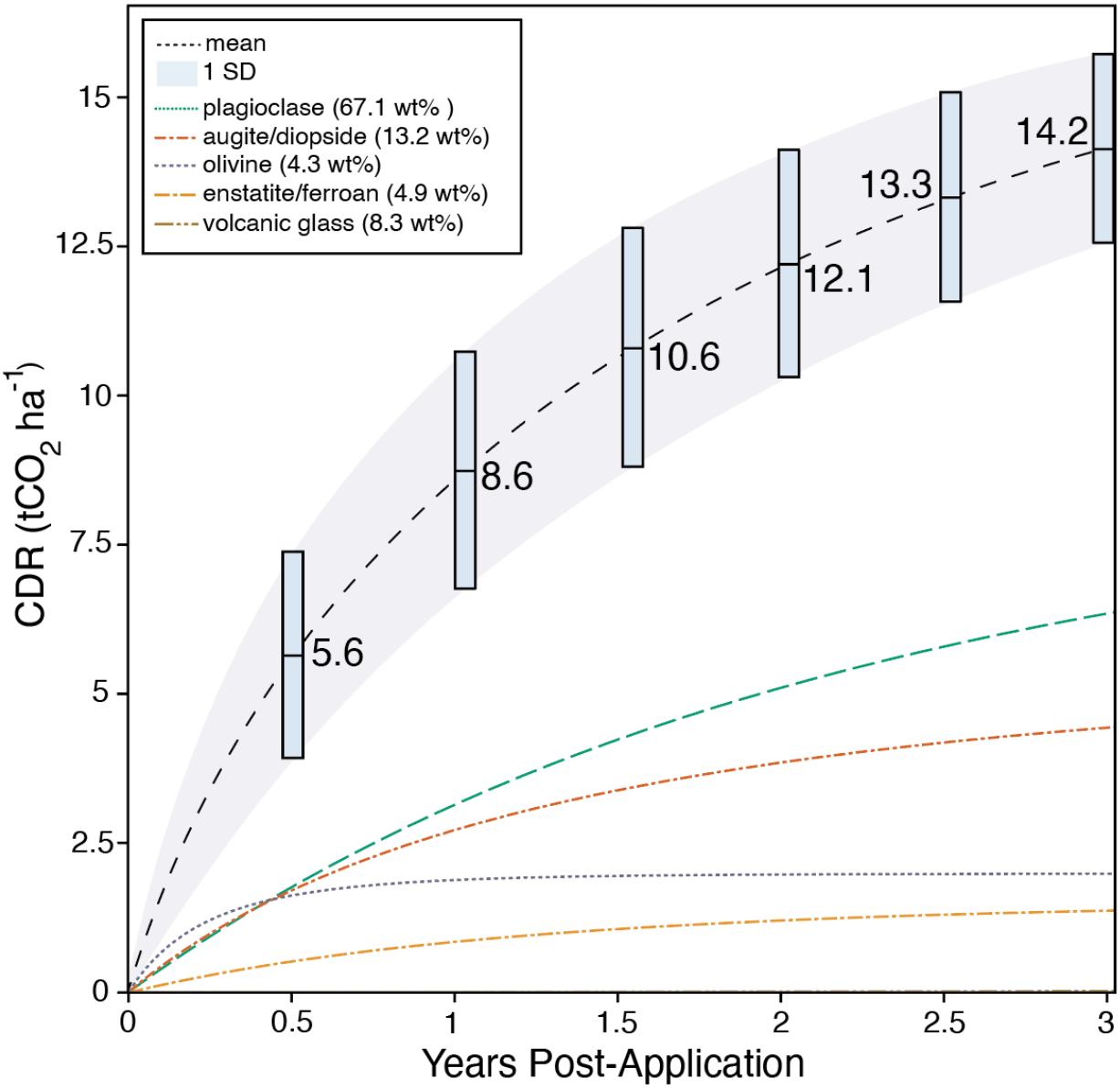

Figure 28. Simplified first-order kinetic model simulating basalt dissolution. Uncertainty is propagated using Monte Carlo simulation (N = 20,000) of ranges in soil pH, temperature, and XRD-derived mineralogy. Colored, dashed curves indicate the dissolution of individual mineral fractions based on a component additivity framework. The sum of these dissolved minerals constitutes the mean dissolution rate (dashed black curve). The shaded region shows a 1 standard deviation uncertainty envelope, with discrete ranges provided every 6 months.